An extended LuGre-brush tyre model for large camber angles and turning speeds

(article starts on next page)

been employed to investigate the nonstationary response of the tyre to time-varying slip and spin inputs. In this context, the first analytical description is due to Schlippe and Segel [13,14], and approximates the behaviour of the tyre carcass with that of a stretched string of infinite length. Over the years, the original formulation has undergone a number of extensions, aimed at improving its accuracy by adding, for example, bristle elements representing the tread, or taking into account the compliance of the tyre in the longitudinal direction [15–17]. Recent contributions have also considered the exact coupled nonlinear kinematics of the rubber particles contacting the ground and the vehicle motion [18–24], and the presence of limited friction inside the tyre contact patch [25–27] according to the classic Coulomb–Amontons assumption [9,10,28–34]. The inherent complexity of modelling the tyre carcass as a distributed system has legitimated the adoption of approximated formulations derived directly from the stretched string models. Amongst these, the *single contact point models* [35–43] constitute a standard approach when it comes to full vehicle dynamics simulations, since they can be easily integrated with Pacejka's Magic Formula (MF) [1,44] or other empirical steady-state tyre formulae. The basic assumption of the single contact point formulation is that the tyre dynamics may be approximated as the one of a linear system, whose main parameter is the so-called *relaxation length*. This is identified as the distance that the tyre needs to travel to develop 63% of the steady-state forces. In this approach, the tyre carcass is held solely responsible for the whole nonstationary process of transient generation of tyre forces and moments. In this way, the dual nature of the tyre is mimicked by a series system that behaves as a spring at low rolling speed and as a damper at high speeds. This pragmatic approach leads to a very straightforward model, which generally shows a good agreement with experimental evidence and – combined with MF, which is currently able to take into account physical phenomena connected to tyre inflation pressure, temperature and wear [45–47] – can also handle the presence of large camber angles and steering speeds. However, two major disadvantages of the single contact point models consist in that they neglect nonstationary phenomena connected to the tread rubber flow inside the contact patch, i.e. the transient of the bristles, and do not come with important dynamical properties, like, e.g. asymptotic and input-to-state stability, that are appetible for control applications.

An alternative approach that is also grounded on the brush theory but accounts for the dynamics of the bristles has been recently developed by the authors and renamed *two-regime* [48]. As opposed to the single contact point formulation, the two-regime models describe the tyre dynamics by means of a nonlinear system of ordinary differential equations directly in terms of forces and moment, and has been proven to be input-to-state stable even in combined slip conditions. On the other hand, an intrinsic difficulty connected to this formulation is the need for local inversion of the steady-state tyre characteristics.

However, being grounded on the stretched string and brush theories, respectively, both the single contact point and two-regime descriptions inherit the drawbacks originating from the Coulomb–Amontons friction model, which may pose some difficulties in the derivation of control-oriented tyre models [49]. Indeed, Coulomb-like friction models imply nonsmooth relationships between the shear stresses acting on the rubber particles contacting the ground and their sliding velocity. In particular, a major disadvantage connects to the possible presence of multiple adhesion and sliding zones inside the contact patch, whose number is unknown *a priori*.

Some of these limitations may be overcome by the LuGre formulation [50], which proposes an alternative friction model to the Coulomb–Amontons one. Indeed, one of the strengths of the LuGre-brush theory resides in that the calculation of the tangential forces generated at the tyre–road interface is carried out by multiplying the normal pressure distribution by a frictional state variable, which may be eventually interpreted as the deformation of a bristle travelling inside the contact patch. This eliminates the need for distinguishing between multiple adhesion and sliding zones. Additional advantages connected to the LuGre friction model are that it predicts correctly not only the Stribeck and pre-sliding displacement effects [50], but also variable breakaway forces and frictional lag phenomena, whereas the traditional brush models notoriously fail. Moreover, being based on linear transport partial differential equations (PDEs), the LuGre formulation (in its standard form) leads to a nicely-behaving dynamical system. In this context, extensive research has already been devoted to incorporating the LuGre model within the brush theory, leading to enhanced tyre models, capable of capturing dynamic effects with high accuracy and extremely suited for control applications [51–57].

With a few exceptions [57], these investigations are however limited to the case of combined translational slips, and systematically disregard the transient effects of the spin, which may play an important role in conditions of large camber angles and steering speeds that are typical of motorsport applications. On the other hand, these effects have been recently investigated by Romano et al. [58–60] taking advantage of the theoretical framework provided by the brush models [1,2,8], under the assumption of vanishing sliding (i.e. virtually infinite friction available inside the contact patch). Specifically, in [58,59], a general procedure to derive the exact analytical solution in the case of time-varying slip inputs was outlined. Then, explicit expressions for the deflection of the bristle were provided for the cases of rectangular and elliptical contact patches. It was also found in [58,59] that vanishing sliding conditions may be treated analytically for many cases of practical interests, whereas, once again, the more stringent situation of limited friction appeared to be a source of further complications when attacking the transient problem, conflicting with the need for simplified nonstationary models to be used in simulation and/or for control purposes. Whilst vanishing sliding conditions are undoubtedly interesting to explore from a theoretical perspective, they are not representative of real tyre operating conditions, therefore limiting the applicability of the results obtained in [58,59].

However, since the structure of the governing PDEs of the standard brush models is similar to that of the LuGre-brush formulation, the intuition and the results obtained in [58,59] may be effectively exploited in the development of an enhanced model for control purposes, and capable of taking correctly into account the individual contributions of the camber and turn spin slips. Therefore, the main scope of this paper is to combine the LuGre friction model with the exact brush theory developed in [58,59]. In this process, the tyre characteristics are obtained as a function of an internal frictional variable, whose dynamics is described using two coupled PDEs. These enjoy important dynamical properties that constitute an essential prerequisite when it comes to designing control algorithms and estimators for distributed dynamical systems. Moreover, although the original formulation in terms of PDEs may eventually be used directly for control-oriented applications [61,62], an approximated description would better serve the purpose. Therefore, starting from the original set of equations, a lumped model is derived that represents the transient tyre forces and moment using multiple sets of simpler ODEs. Similar approximations are

well documented in the literature [51–57] and describe the tyre dynamics using aggregate frictional states, which may be interpreted as global or averaged variables inside the contact patch.

Whilst possible disadvantages and improvements of the LuGre model have been discussed in [63–67], where enhanced descriptions have also been proposed based on refined friction models [65,68], the adoption of the LuGre-brush formulation in this paper is justified by its almost ubiquitous presence in the vast control-oriented literature in the field [69–74], together with its nice properties and relative simplicity, which allow for natural extensions in several research directions. In this context, it should be also observed that the present work is mainly theoretical in nature and should be intended as a starting point for future investigations.

The remainder of the manuscript is organised as follows: Section 2 introduces the governing equations of the LuGre-brush tyre models, and states the corresponding boundary (BCs) and initial conditions (ICs); Section 3 derives the closed-form solutions for the time-varying frictional state in case of constant slip inputs and compares the resulting steady-state tyre characteristics against the standard version of the LuGre tyre model and the exact brush theory for large camber angles presented in [58,59]. The development of the approximated lumped models for the tyre characteristics is instead carried out in Section 5. Finally, Section 6 summarises the main findings of the paper and outlines future directions for research.

2. The LuGre-brush tyre model

In this paper, the governing equations of the brush models according to the LuGre formulation are divided in three sets: the *kinematic equations*, the *friction relationship* and the *equilibrium equations*.

2.1. Kinematic equations

The kinematic equations relate the time derivative of the internal frictional state $z(x, t)$ to the local sliding velocity[1] $v_\mu(x, t)$ between the tyre and the road:

$$\frac{\partial z(x,t)}{\partial t} + \big(v_t(x,t) \cdot \nabla_t\big)z(x,t) = v_\mu\big(z(x,t),x,t\big)$$

$$- \frac{v_\mu\big(z(x,t),x,t\big)}{g\Big(v_\mu\big(z(x,t),x,t\big)\Big)}\mathbf{C}_0 z(x,t), \quad (x,t) \in \overset{\circ}{\mathscr{P}} \times \mathbb{R}_{>0}, \tag{1}$$

where $\overset{\circ}{\mathscr{P}}$ denotes the interior of the contact patch $\mathscr{P}$, modelled as a compact subset of the road plane Π and assumed fixed for simplicity, $v_\mu(z(x,t),x,t) \triangleq \big\|v_\mu(z(x,t),x,t)\big\|$ and

$$\mathbf{C}_0 = \begin{bmatrix} c_{0xx} & c_{0xy} \\ c_{0yx} & c_{0yy} \end{bmatrix} \tag{2}$$

is a constant matrix, often assumed to be positive-definite or even diagonal. It may be noticed that the entries of the matrix $\mathbf{C}_0$ have the same dimension of a curvature. The

sliding function $g(v_\mu(z(x,t),x,t))$ in Equation (1) is usually postulated in the form

$$g\Big(v_\mu\big(z(x,t),x,t\big)\Big) = \mu_d + \big(\mu_s - \mu_d\big)\,e^{-\big(v_\mu(z(x,t),x,t)/v_\delta\big)^\delta}, \tag{3}$$

where μ_s and μ_d are the static and dynamic friction coefficients, clearly with $\mu_d \leq \mu_s$, v_δ is the *Stribeck velocity*, and δ is the *Stribeck exponent*. It should be observed that μ_d and μ_s are global quantities in the LuGre friction model, meaning that they are not function of the position inside the contact patch $\mathscr{P}$.

In particular, from the exact formulation of the brush theory, the sliding velocity $v_\mu(x,t) = V_r(t)\bar{v}_\mu(x,t)$ and the tangential velocity field $v_t(x,t) = V_r(t)\bar{v}_t(x,t)$ may be derived as follows:

$$\bar{v}_\mu(x,t) = \sigma(t) + \mathbf{A}_\varphi(t)\big(x + \chi_\psi(t)z(x,t)\big), \tag{4}$$

and

$$\bar{v}_t(x,t) = -\begin{bmatrix} 1 \\ 0 \end{bmatrix} + \mathbf{A}_{\varphi_\gamma}(t)x, \tag{5}$$

where $V_r(t) = \Omega(t)R_r(t)$ is the so-called *rolling speed* of the tyre, $\Omega(t)$ is the angular speed of the wheel hub around its axis, $R_r(t)$ is the so-called *rolling radius*, $\sigma(t) = \begin{bmatrix} \sigma_x(t) & \sigma_y(t) \end{bmatrix}^\mathrm{T}$ is the vector of *translational slips*, and the *spin* and *camber tensors* $\mathbf{A}_\varphi(t)$, $\mathbf{A}_{\varphi_\gamma}(t)$ write respectively as

$$\mathbf{A}_\varphi(t) = \begin{bmatrix} 0 & -\varphi(t) \\ \varphi(t) & 0 \end{bmatrix}, \tag{6a}$$

$$\mathbf{A}_{\varphi_\gamma}(t) = \begin{bmatrix} 0 & \varphi_\gamma(t) \\ -\varphi_\gamma(t) & 0 \end{bmatrix}. \tag{6b}$$

The spin variable $\varphi(t)$ appearing in the spin tensor accounts for both the turning speed of the tyre $\dot{\psi}(t)$ around its axis and the vertical component of the rolling velocity due to camber $\gamma(t)$. Hence, it may be generally decomposed as $\varphi(t) = \varphi_\gamma(t) + \varphi_\psi(t)$, with

$$\varphi_\gamma(t) = \frac{1}{R_r}\big(1 - \varepsilon_\gamma\big)\sin\gamma(t), \tag{7a}$$

$$\varphi_\psi(t) = -\frac{\dot{\psi}(t)}{V_r(t)}. \tag{7b}$$

The variables $\varphi_\gamma(t)$ and $\varphi_\psi(t)$ are called *camber* and *turn spin*, respectively. They may be interpreted as two different signed curvatures $\varphi_\gamma = 1/R_\gamma$ and $\varphi_\psi = -1/R_\psi$; the actual curvature of the contact patch centre is thus given by the difference $\varphi = 1/R_\gamma - 1/R_\psi$. The camber and turn spin slips may be conveniently expressed as ratios of the total spin, that is $\varphi_\gamma = \chi_\gamma\varphi$ and $\varphi_\psi = \chi_\psi\varphi$, with $\chi_\gamma + \chi_\psi = 1$. The coefficients χ_γ and χ_ψ have been introduced by Romano et al. [58] and are called *camber* and *turn ratio*, respectively.

Finally, the quantity ε_γ in Equation (7a) is known as *camber reduction factor* and incorporates additional curvature effects due to ply-steer and conicity. For car and truck tyres,

this parameter ranges between 0.4 and 0.7, whilst motorcycle tyres have camber reduction factor $\varepsilon_\gamma \approx 0$ [1,2,8,75].

Equations (1), (4), (6a) together yield the general form for the governing PDEs of the LuGre-brush tyre model for large camber angles and turning speeds. However, in this formulation, they do not admit analytical solution for the frictional state $z(x, t)$, as also reported by Deur [57]. This is due to the fact that, according to Equations (3) and (4), the sliding function $g(\cdot)$ and the total velocity $v_\mu(z(x, t), x, t)$ depend not only on the vector position inside the contact patch but also on the frictional state itself. Therefore, to derive a closed-form expression for $z(x, t)$, at least in steady-state conditions, this paper approximates the original PDEs as

$$\frac{\partial z(x, t)}{\partial t} + \big(v_t(x, t) \cdot \nabla_t\big)z(x, t) = V_r(t)\Big[\sigma(t) + A_\varphi(t)\big(x + \chi_\psi(t)z(x, t)\big)\Big]$$
$$- \frac{\hat{v}_\mu(t)}{g(\hat{v}_\mu(t))}C_0 z(x, t), \quad (x, t) \in \mathring{\mathscr{P}} \times \mathbb{R}_{>0}, \quad (8)$$

where $\hat{v}_\mu(t)$ is calculated by neglecting the contribution $A_{\varphi_\psi}(t)z(x, t)$ in Equation (4), and considering average values for the longitudinal and lateral components of $v_\mu(x, t)$. It is also worth observing that, for a symmetrical contact patch, it is $\hat{v}_\mu(t) \equiv V_r(t)\sigma(t)$, with $\sigma(t) \triangleq \|\sigma(t)\|$. Some qualitative results for the more general case in which $\hat{v}_\mu(x, t)$ is assumed to vary with the coordinate x, but not with $z(x, t)$, are instead presented in Appendix 1 (see Remark A.2).

The vector Equation (8) is composed of two linear transport PDEs and comes equipped with BC and IC given respectively by

$$\text{BC}: \quad z(x, t) = 0, \quad (x, t) \in \mathscr{L} \times \mathbb{R}_{>0}, \quad (9a)$$

$$\text{IC}: \quad z(x, 0) = z_0(x), \quad x \in \mathring{\mathscr{P}}, \quad (9b)$$

possibly for some $z_0(x) \in C^1(\mathring{\mathscr{P}}; \mathbb{R}^2)$ with $z_0(x) = 0$ on $\mathscr{L}$. The IC (9b) specifies an initial distribution $z_0(x)$ for the frictional state, whilst the BC (9a) prescribes that the frictional state must vanish on the leading edge $\mathscr{L}$. The notion of leading edge strictly connects to those of *neutral edge* and *trailing edge*, according to the following Definition 2.1.

Definition 2.1 (Leading edge, neutral edge and trailing edge for fixed contact patch): Assuming a fixed contact shape, the leading, neutral and trailing edges $\mathscr{L}$, $\mathscr{N}$ and $\mathscr{T}$ are defined respectively by

$$\mathscr{L} \triangleq \big\{x \in \partial\mathscr{P} \mid v_t(x, t) \cdot \hat{v}_{\partial\mathscr{P}}(x) < 0\big\}, \quad (10a)$$

$$\mathscr{N} \triangleq \big\{x \in \partial\mathscr{P} \mid v_t(x, t) \cdot \hat{v}_{\partial\mathscr{P}}(x) = 0\big\}, \quad (10b)$$

$$\mathscr{T} \triangleq \big\{x \in \partial\mathscr{P} \mid v_t(x, t) \cdot \hat{v}_{\partial\mathscr{P}}(x) > 0\big\}, \quad (10c)$$

where $\partial\mathscr{P}$ is the boundary of the contact patch, $\hat{v}_{\partial\mathscr{P}}(x)$ is the outward-pointing unit normal to the boundary $\partial\mathscr{P}$ of the contact patch.

Definition 2.1 may be extended to the more general case of time-varying contact geometry as in Ref. [59].

2.2. Friction relationship

In the LuGre friction model, the local friction coefficient $\boldsymbol{\mu}(\boldsymbol{x}, t) = \left[\mu_x(\boldsymbol{x}, t) \ \mu_y(\boldsymbol{x}, t)\right]^{\mathrm{T}}$ inside the contact patch depends on the internal state $\boldsymbol{z}(\boldsymbol{x}, t)$ according to the following relationship:

$$\boldsymbol{\mu}(\boldsymbol{x}, t) = \mathbf{C}_0 \boldsymbol{z}(\boldsymbol{x}, t) + \mathbf{C}_1 \frac{\partial \boldsymbol{z}(\boldsymbol{x}, t)}{\partial t} + \mathbf{C}_2 \boldsymbol{v}_\mu(\boldsymbol{x}, t), \tag{11}$$

where $\mathbf{C}_1, \mathbf{C}_2$ are two matrices of constant coefficients:

$$\mathbf{C}_1 = \begin{bmatrix} c_{1xx} & c_{1xy} \\ c_{1yx} & c_{1yy} \end{bmatrix}, \tag{12a}$$

$$\mathbf{C}_2 = \begin{bmatrix} c_{2xx} & c_{2xy} \\ c_{2yx} & c_{2yy} \end{bmatrix}, \tag{12b}$$

usually assumed to be positive definite and even diagonal. Their entries are expressed in $\mathrm{s\,m^{-1}}$.

2.3. Equilibrium equations

In the LuGre formulation, the tangential forces exerted at the tyre–road interface are given by the product between the local friction coefficient $\boldsymbol{\mu}(\boldsymbol{x}, t)$ and the normal pressure distribution $q_z(\boldsymbol{x}, t)$, expressed in $\mathrm{N\,m^{-2}}$. Integrating over the contact patch $\mathscr{P}$ yields the following expressions for the tangential force vector $\boldsymbol{F_t}(t) = \left[F_x(t) \ F_y(t)\right]^{\mathrm{T}}$ and the self-aligning moment $M_z(t)$:

$$\boldsymbol{F_t}(t) = \iint_{\mathscr{P}} \boldsymbol{\mu}(\boldsymbol{x}, t) q_z(\boldsymbol{x}) \, \mathrm{d}\boldsymbol{x}, \tag{13a}$$

$$M_z(t) = \iint_{\mathscr{P}} \left(x\mu_y(\boldsymbol{x}, t) - y\mu_x(\boldsymbol{x}, t)\right) q_z(\boldsymbol{x}) \, \mathrm{d}\boldsymbol{x}. \tag{13b}$$

Equations (13a) are known as *equilibrium equations*. It should be observed that, according to Equation (13b), the self-aligning moment is computed on the undeformed configuration.

3. Analytical solutions for constant slip inputs

In the general case of time-varying slip inputs and contact patch, Equation (8) admits integral solutions in parametric form. These may be easily found by resorting to the classic method of characteristic lines for partial differential equations, as discussed in detail in [59]. However, closed-form expressions for the frictional state $\boldsymbol{z}(\boldsymbol{x}, t)$ are usually only possible when the spin slips are constant and the shape of the contact patch admits simple analytical representations. Therefore, to limit the scope of this paper, only the case where the slip inputs and rolling speed are constant over time is considered. Moreover, the rolling speed is assumed to be always positive, so that the mapping between the travelled distance

$s = \int_0^t V_\mathrm{r}(t')\,\mathrm{d}t'$ and the time is one-to-one. Owing to these premises, replacing the time variable t with the travelled distance s turns Equation (8) into

$$\frac{\partial \boldsymbol{z}(\boldsymbol{x},s)}{\partial s} + \big(\bar{\boldsymbol{v}}_t(\boldsymbol{x}) \cdot \nabla_t\big)\boldsymbol{z}(\boldsymbol{x},s) = \boldsymbol{\sigma} + \mathbf{A}_\varphi\big(\boldsymbol{x} + \chi_\psi \boldsymbol{z}(\boldsymbol{x},s)\big)$$

$$- \frac{\hat{v}_\mu}{V_\mathrm{r}g(\hat{v}_\mu)}\,\mathbf{C}_0 \boldsymbol{z}(\boldsymbol{x},s), \quad (\boldsymbol{x},s) \in \mathring{\mathscr{P}} \times \mathbb{R}_{>0}. \tag{14}$$

Renaming

$$\begin{bmatrix} \varphi_{xx} & \varphi_{xy} \\ \varphi_{yx} & \varphi_{yy} \end{bmatrix} \triangleq \frac{\hat{v}_\mu}{V_\mathrm{r}g(\hat{v}_\mu)} \begin{bmatrix} c_{0xx} & c_{0xy} \\ c_{0yx} & c_{0yy} \end{bmatrix} = \frac{\hat{v}_\mu}{V_\mathrm{r}g(\hat{v}_\mu)}\mathbf{C}_0, \tag{15}$$

and assuming parametrisations of the type $\boldsymbol{x} = \boldsymbol{x}(\boldsymbol{\rho},\varsigma)$, $s = \boldsymbol{x}(\boldsymbol{\rho},\varsigma)$ and $\boldsymbol{z} = \boldsymbol{z}(\boldsymbol{x}(\boldsymbol{\rho},\varsigma),\boldsymbol{x}(\boldsymbol{\rho},\varsigma)) = \boldsymbol{\zeta}(\boldsymbol{\rho},\varsigma)$, for constant slip inputs and rolling speeds the original PDEs may be restated as

$$\frac{\mathrm{d}s(\boldsymbol{\rho},\varsigma)}{\mathrm{d}\varsigma} = 1, \tag{16a}$$

$$\frac{\mathrm{d}\boldsymbol{x}(\boldsymbol{\rho},\varsigma)}{\mathrm{d}\varsigma} = -\begin{bmatrix} 1 \\ 0 \end{bmatrix} + \mathbf{A}_{\varphi_\gamma}\boldsymbol{x}(\boldsymbol{\rho},\varsigma), \tag{16b}$$

$$\frac{\mathrm{d}\boldsymbol{\zeta}(\boldsymbol{\rho},\varsigma)}{\mathrm{d}\varsigma} = \tilde{\mathbf{A}}_{\varphi_\psi}\boldsymbol{\zeta}(\boldsymbol{\rho},\varsigma) + \boldsymbol{\sigma} + \mathbf{A}_\varphi\boldsymbol{x}(\boldsymbol{\rho},\varsigma), \tag{16c}$$

where the *modified turn spin tensor* has been defined as

$$\tilde{\mathbf{A}}_{\varphi_\psi} \triangleq \mathbf{A}_{\varphi_\psi} - \frac{\hat{v}_\mu}{V_\mathrm{r}g(\hat{v}_\mu)}\mathbf{C}_0 = \begin{bmatrix} -\varphi_{xx} & -\varphi_\psi - \varphi_{xy} \\ \varphi_\psi - \varphi_{yx} & -\varphi_{yy} \end{bmatrix}. \tag{17}$$

The solution to the above system (16a) may be derived as explained in Romano et al. [59] and reads

$$s(\boldsymbol{\rho},\varsigma) = \varsigma + s_0(\boldsymbol{\rho}), \tag{18a}$$

$$\boldsymbol{x}(\boldsymbol{\rho},\varsigma) = \mathbf{R}_{\varphi_\gamma}(\varsigma)\big(\boldsymbol{x}_0(\boldsymbol{\rho}) - \boldsymbol{x}_{C_\gamma}\big) + \boldsymbol{x}_{C_\gamma}, \tag{18b}$$

$$\boldsymbol{\zeta}(\boldsymbol{\rho},\varsigma) = \tilde{\Phi}_{\varphi_\psi}(\varsigma,0)\big(\boldsymbol{\zeta}_0(\boldsymbol{\rho}) - \tilde{\boldsymbol{\xi}}_0(\boldsymbol{\rho})\big) + \tilde{\boldsymbol{\zeta}}(\boldsymbol{\rho},\varsigma). \tag{18c}$$

Equations (18a) and (18b) relate the physical variables $(\boldsymbol{x},s)$ to the parametric coordinates $(\boldsymbol{\rho},\varsigma)$. In particular, Equation (18a) is a transformation between time-like variables, whilst Equation (18b) parametrises the trajectories of the rubber flow inside the contact patch. If the frictional state $\boldsymbol{z}(\boldsymbol{x},s)$ is interpreted as the deflection of a bristle, then Equation (18b) clearly describes the kinematics of its root attached to the tyre. Specifically, $\mathbf{R}_{\varphi_\gamma}(\varsigma)$ in

Equation (18b) is the so-called *camber rotation matrix*, given by

$$\mathbf{R}_{\varphi_\gamma}(\varsigma) = e^{\mathbf{A}_{\varphi_\gamma}\varsigma} = \begin{bmatrix} \cos(\varphi_\gamma\varsigma) & \sin(\varphi_\gamma\varsigma) \\ -\sin(\varphi_\gamma\varsigma) & \cos(\varphi_\gamma\varsigma) \end{bmatrix}, \tag{19}$$

whilst the vector

$$\boldsymbol{x}_{C_\gamma} = \begin{bmatrix} 0 & y_{C_\gamma} \end{bmatrix}^{\mathrm{T}} \triangleq \begin{bmatrix} 0 & R_\gamma \end{bmatrix}^{\mathrm{T}} = \begin{bmatrix} 0 & 1/\varphi_\gamma \end{bmatrix}^{\mathrm{T}} \tag{20}$$

denotes the position of the *cambering centre* C_γ. Equation (18c) describes instead the dynamics of the transformed internal state $\boldsymbol{\zeta}(\boldsymbol{\rho}, \varsigma)$. Specifically, the entries of the *modified turning transition matrix*

$$\tilde{\boldsymbol{\Phi}}_{\varphi_\psi}(\varsigma, 0) = e^{\tilde{\mathbf{A}}_{\varphi_\psi}\varsigma} = \begin{bmatrix} \phi_{\varphi_\psi 11}(\varsigma) & \phi_{\varphi_\psi 12}(\varsigma) \\ \phi_{\varphi_\psi 21}(\varsigma) & \phi_{\varphi_\psi 22}(\varsigma) \end{bmatrix} \tag{21}$$

write as follows:

$$\phi_{\varphi_\psi 11}(\varsigma) = \frac{(\varphi_{xx} - \varphi_{yy})\phi_1(\varsigma) + \tilde{\varphi}_\psi\phi_2(\varsigma)}{2\tilde{\varphi}_\psi}, \tag{22a}$$

$$\phi_{\varphi_\psi 12}(\varsigma) = -\frac{2e^{-\frac{(\varphi_{xx}+\varphi_{yy})\varsigma}{2}}\sinh\left(\frac{\tilde{\varphi}_\psi\varsigma}{2}\right)(\varphi_{xy} + \varphi_\psi)}{\tilde{\varphi}_\psi}, \tag{22b}$$

$$\phi_{\varphi_\psi 21}(\varsigma) = -\frac{e^{-\frac{(\varphi_{xx}+\varphi_{yy}+\tilde{\varphi}_\psi)\varsigma}{2}}\left(e^{\tilde{\varphi}_\psi\varsigma} - 1\right)(\varphi_{yx} - \varphi_\psi)}{\tilde{\varphi}_\psi}, \tag{22c}$$

$$\phi_{\varphi_\psi 22}(\varsigma) = \frac{(\varphi_{yy} - \varphi_{xx})\phi_1(\varsigma) + \tilde{\varphi}_\psi\phi_2(\varsigma)}{2\tilde{\varphi}_\psi}, \tag{22d}$$

with the functions $\phi_1(\cdot)$, $\phi_2(\cdot)$ reading

$$\phi_1(\varsigma) \triangleq e^{-\frac{(\varphi_{xx}+\varphi_{yy}+\tilde{\varphi}_\psi)\varsigma}{2}} - e^{-\frac{(\varphi_{xx}+\varphi_{yy}-\tilde{\varphi}_\psi)\varsigma}{2}}, \tag{23a}$$

$$\phi_2(\varsigma) \triangleq e^{-\frac{(\varphi_{xx}+\varphi_{yy}+\tilde{\varphi}_\psi)\varsigma}{2}} + e^{-\frac{(\varphi_{xx}+\varphi_{yy}-\tilde{\varphi}_\psi)\varsigma}{2}}, \tag{23b}$$

and

$$\tilde{\varphi}_\psi \triangleq \sqrt{(\varphi_{xx} - \varphi_{yy})^2 - 4(\varphi_\psi + \varphi_{xy})(\varphi_\psi - \varphi_{yx})}. \tag{24}$$

It may be easily verified that the transition matrix $\tilde{\boldsymbol{\Phi}}_{\varphi_\psi}(\varsigma, 0)$ in Equation (21) reduces to a rotation matrix when $\varphi_{xx} = \varphi_{xy} = \varphi_{yx} = \varphi_{yy} = 0$, yielding exactly the same result of the exact brush theory presented in [58,59]. The function $\tilde{\boldsymbol{\zeta}}(\cdot, \cdot)$ appearing in Equation (18c) may be expressed in matrix form as

$$\tilde{\boldsymbol{\zeta}}(\boldsymbol{\rho}, \varsigma) = \begin{bmatrix} \alpha_{xx} & \alpha_{xy} \\ \alpha_{yx} & \alpha_{yy} \end{bmatrix} \boldsymbol{x}(\boldsymbol{\rho}, \varsigma) + \begin{bmatrix} \beta_x \\ \beta_y \end{bmatrix}, \tag{25}$$

where the coefficients $\alpha_{xx}, \alpha_{xy}, \alpha_{yx}, \alpha_{yy}, \beta_x$ and β_y depend in turn upon $\boldsymbol{\sigma}, \varphi_\gamma, \varphi_\psi$ and V_r. Their expressions are quite lengthy and reported in Appendix A.1. Finally, $\tilde{\boldsymbol{\zeta}}_0(\boldsymbol{\rho}) \triangleq \tilde{\boldsymbol{\zeta}}(\boldsymbol{\rho}, 0)$ in Equation (18c).

To derive the analytical expression for the frictional state $z(x, s)$, a mapping between the parametric coordinates (ρ, ς) and the initial variables (x, s) should be found so to transform back the function $\zeta(\rho, \varsigma)$ [76–78]. This may be done prescribing in turn the BC (9a) and IC (9b), respectively, which guarantee the uniqueness of a diffeomorphism between the coordinates (ρ, ς) and (x, s), and thus also the uniqueness of the solution for the problem at hand, at least locally. Similar considerations about the importance of the inflow BC may be drawn from an application of the energy method, as reported in Appendix 1, where the inflow BC plays again a fundamental role.

In particular, enforcing (9a) and (9b) yields two different solutions for $z(x, s)$, corresponding to the steady-state and transient one, denoted by $z^-(x)$ and $z^+(x, s)$, and defined respectively on the subdomains $\mathscr{P}^-$ and $\mathscr{P}^+$ of the contact patch. The global solution over the contact patch $\mathscr{P} = \mathscr{P}^- \cup \mathscr{P}^+$ may be then formally constructed as

$$z(x, s) = \begin{cases} z^-(x), & (x, s) \in \mathscr{P}^- \times \mathbb{R}_{\geq 0}, \\ z^+(x, s), & (x, s) \in \mathscr{P}^+ \times \mathbb{R}_{\geq 0}. \end{cases} \tag{26}$$

Sections 3.1 and 3.2 are dedicated to the derivation of the steady-state and transient solutions $z^-(x)$ and $z^+(x, s)$ for the frictional state.

3.1. Steady-state solution

The steady-state solution for the frictional state $z^-(x, s)$ should be sought by enforcing the BC (9a), which imposes $z(x, s) = 0$ on the leading edge $\mathscr{L}$. Compatibility conditions imply therefore $\zeta_0(\rho) = 0$. By noticing that

$$\tilde{\zeta}\big(\rho(x, s), \varsigma(x, s)\big) = \tilde{z}(x) \triangleq \begin{bmatrix} \alpha_{xx} & \alpha_{xy} \\ \alpha_{yx} & \alpha_{yy} \end{bmatrix} x + \begin{bmatrix} \beta_x \\ \beta_y \end{bmatrix}, \tag{27}$$

and manipulating Equations (18a), (18b) as

$$x^2 + \big(y - 1/\varphi_\gamma\big)^2 = \big(x_0(\rho)\big)^2 + \big(y_0(\rho) - 1/\varphi_\gamma\big)^2, \tag{28a}$$

$$\varsigma = \frac{1}{\varphi_\gamma} \left[\arctan\left(\frac{x}{y - 1/\varphi_\gamma}\right) - \arctan\left(\frac{x_0(\rho)}{y_0(\rho) - 1/\varphi_\gamma}\right) \right], \tag{28b}$$

$$s_0(\rho) = s - \varsigma, \tag{28c}$$

the following representation formula may be obtained for the frictional state in the steady-state region $\mathscr{P}^-$ of the contact patch:

$$z^-(x) = \tilde{\Phi}_{\varphi_\psi}\big(\Sigma(x), 0\big)\Psi(x) + \tilde{z}(x), \quad (x, s) \in \mathscr{P}^- \times \mathbb{R}_{\geq 0}. \tag{29}$$

In particular, it should be noticed that, owing to the assumption of constant slips and fixed contact patch, the initial conditions for the independent variables s and x may be parametrised independently as $s_0(\rho) = \rho_1$ and $x_0(\rho) = x_0(\rho_2)$, respectively. Accordingly, the functions $\Sigma(\cdot)$ and $\Psi(\cdot)$ appearing in Equation (29) are as follows:

$$\Sigma(x) \triangleq \frac{1}{\varphi_\gamma} \left[\arctan\left(\frac{x}{y - 1/\varphi_\gamma}\right) - \arctan\left(\frac{x_0\big(\rho_2(x)\big)}{y_0\big(\rho_2(x)\big) - 1/\varphi_\gamma}\right) \right], \tag{30a}$$

$$\boldsymbol{\Psi}(\boldsymbol{x}) = \begin{bmatrix} \Psi_x(\boldsymbol{x}) & \Psi_y(\boldsymbol{x}) \end{bmatrix}^{\mathrm{T}} \triangleq -\tilde{z}\Big(\boldsymbol{x}_0\big(\rho_2(\boldsymbol{x})\big)\Big), \tag{30b}$$

where the expressions for $\boldsymbol{x}_0(\boldsymbol{\rho}) = \boldsymbol{x}_0(\rho_2)$ should be derived starting from an analytical representation of the leading edge. In particular, the exact functions for $\boldsymbol{x}_0(\boldsymbol{\rho}) = \boldsymbol{x}_0(\rho_2)$ have been derived by Romano et al. [59] for a rectangular and elliptical contact patch, and are reported in Appendix A.2 for completeness. From Equation (29), it may also be observed that $\boldsymbol{z}^-(\boldsymbol{x})$ is independent of the travelled distance, as it happens in the basic formulation of the brush models.

Finally, it is worth mentioning that, in Equation (29), the domain $\mathscr{P}^-$ is defined from the requirement $s_0(\rho_1(\boldsymbol{x}, s)) = \rho_1(\boldsymbol{x}, s) > 0$ of Equation (28c). Together with (28b), which gives $s > \Sigma(\boldsymbol{x})$, this yields

$$\gamma_\Sigma(\boldsymbol{x}, s) \triangleq \Sigma(\boldsymbol{x}) - s. \tag{31}$$

Therefore, the subset $\mathscr{P}^-$ of $\mathscr{P}$, describing the stationary region of the contact patch, may be defined mathematically as

$$\mathscr{P}^- \triangleq \big\{\boldsymbol{x} \in \mathscr{P} \mid \gamma_\Sigma(\boldsymbol{x}, s) < 0\big\}. \tag{32}$$

In particular, the curve parametrised by $\gamma_\Sigma(\boldsymbol{x}, s) = 0$ is referred to as *transient* or *travelling edge* in [59].

3.2. Transient solution

The transient solution $\boldsymbol{z}^+(\boldsymbol{x}, s)$ applies to the transient region of the contact patch:

$$\mathscr{P}^+ \triangleq \big\{\boldsymbol{x} \in \mathscr{P} \mid \gamma_\Sigma(\boldsymbol{x}, s) \geq 0\big\}. \tag{33}$$

The analytical expression for $\boldsymbol{z}^+(\boldsymbol{x}, s)$ may be obtained by parametrising $\boldsymbol{x}_0(\boldsymbol{\rho}) = \boldsymbol{\rho}$ for $s_0(\boldsymbol{\rho}) = 0$. Specifically, it follows again from compatibility that $\boldsymbol{\zeta}_0(\boldsymbol{\rho}(\boldsymbol{x}, s)) = \boldsymbol{z}_0(\boldsymbol{x}_0(\boldsymbol{x}, s))$, and therefore the transient solution is given by

$$\boldsymbol{z}^+(\boldsymbol{x}, s) = \tilde{\Phi}_{\varphi_\psi}(s, 0)\Big[\boldsymbol{z}_0\big(\boldsymbol{x}_0(\boldsymbol{x}, s)\big) - \tilde{\boldsymbol{z}}_0(\boldsymbol{x}, s)\Big] + \tilde{\boldsymbol{z}}(\boldsymbol{x}), \quad (\boldsymbol{x}, s) \in \mathscr{P}^+ \times \mathbb{R}_{\geq 0}, \tag{34}$$

where $\tilde{\boldsymbol{z}}_0(\boldsymbol{x}, s) \triangleq \tilde{\boldsymbol{z}}(\boldsymbol{x}_0(\boldsymbol{x}, s))$ and

$$\boldsymbol{x}_0(\boldsymbol{x}, s) = \boldsymbol{\rho}(\boldsymbol{x}, s) = \mathbf{R}_{\varphi_\gamma}^{-1}(s)\big(\boldsymbol{x} - \boldsymbol{x}_{C_\gamma}\big) + \boldsymbol{x}_{C_\gamma}. \tag{35}$$

The solution constructed by patching the steady-state and transient states according to Equation (26) is clearly continuous on the travelling edge, that is $\boldsymbol{z}^+(\boldsymbol{x}, \Sigma(\boldsymbol{x})) \equiv \boldsymbol{z}^-(\boldsymbol{x})$.

4. Steady-state tyre characteristics

Starting from the closed-form solutions for the internal frictional state, the steady-state tyre characteristics may be obtained integrating numerically over the contact patch according to Equation (13a). In this section, the tyre forces and moment are compared to those obtained using the classic LuGre-brush formulation and the exact brush theory recently developed by the authors in [58,59].

### 4.1. Comparison with the classic LuGre-brush tyre models

Figure 1 compares the stationary tyre forces and moment for a rectangular contact patch for different translational slip inputs $\boldsymbol{\sigma}$ and a fixed spin $\varphi = 3.33 \text{ m}^{-1}$ (with $\chi_\gamma = 0.9$) according to both the LuGre-brush theory for large camber angles presented in this paper and the classic one (Appendix 3). Specifically, Figure 1 was produced considering a contact patch with semilength and semiwidth of $a = 0.075$ and $b = 0.05$ m, respectively. The vertical force acting upon the tyre was set to $F_z = 3000$ N, whilst the matrix $\mathbf{C}_0$ was assumed to be diagonal with $c_{0xx} = c_{0yy} = 240 \text{ m}^{-1}$. Generally speaking, a good qualitative agreement between the two formulations may be observed, which would eventually confirm the accuracy of the LuGre-brush tyre model even in its standard version. However, the novel formulation tends apparently to predict slightly larger forces. In this context, it is also important to mention that, whilst the classic LuGre-brush theory yields a unique steady-state solution $\boldsymbol{z}^-(\boldsymbol{x}) \in C^1(\mathring{\mathscr{P}}^- \times \mathbb{R}_{>0}; \mathbb{R}^2)$ over the entire contact patch, the model for large camber angles predicts the existence of three different analytical functions describing the internal frictional state inside as many subdomains of $\mathscr{P}$, as better explained in Appendix A.2.

Similar considerations hold also true for the tyre characteristics of an elliptical contact patch illustrated in Figure 2. In generating the curves in Figure 2, the same tyre parameters were assumed as for Figure 1, except $c_{0xx} = c_{0yy} = 320 \text{ m}^{-1}$. Perhaps, a substantial difference from the trends plotted in Figure 1 is that the self-aligning moment exhibits a local maximum for positive values of the lateral slip σ_y. This phenomenon is a minor effect linked to the aspect ratio a/b of the contact ellipse. In particular, the fulfilment of the condition $a \leq b(b + 1/\left|\varphi_\gamma\right|)$ guarantees a solution $\boldsymbol{z}(\boldsymbol{x})^- \in C^1(\mathring{\mathscr{P}}^- \times \mathbb{R}_{>0}; \mathbb{R}^2)$ defined on the entire contact patch.

4.2. Comparison with the exact brush tyre models

A comparison between the tyre characteristics predicted by the LuGre-brush theory for large camber angles and the exact brush models presented in [58,59] is shown in Figure 3 for a rectangular contact patch, where the trend of the forces and moment is plotted versus the longitudinal slip σ_x, for several fixed values of the lateral slip input σ_y. Again, in generating Figure 3, a total spin slip of $\varphi = 3.33 \text{ m}^{-1}$ was considered. The stiffnesses and the geometrical parameters were also set as in Section 4.1. The stiffness of the bristle according to the exact brush theory was instead chosen as $2.67 \cdot 10^7 \text{ N m}^{-3}$. Specifically, this value was slightly adjusted starting from the one that, in pure slip conditions, ensures that the derivative of the tyre forces at the origin, i.e. the slip stiffness, is the same for both formulation.[2] To provide a fair comparison, the static and friction coefficients were also assumed to be equal, that is $\mu_s \equiv \mu_d$ in Equation (3).

Opposed to what observed from the comparison between the enhanced and classic LuGre formulations, the discrepancy with the exact brush theory (solid lines) is particularly significant, especially at low values of the lateral slip σ_y, where the LuGre-brush model (dashed lines) for large camber angles tends to predict much higher lateral forces F_y and self-aligning moments M_z. In respect to the lateral force, this phenomenon may be easily explained by noticing that, in the standard brush tyre models, the shear stresses acting upon the bristles are always constrained below the traction bound[3] $\mu_s q_z(\boldsymbol{x})$, and therefore
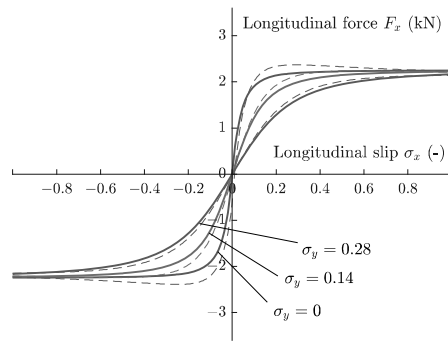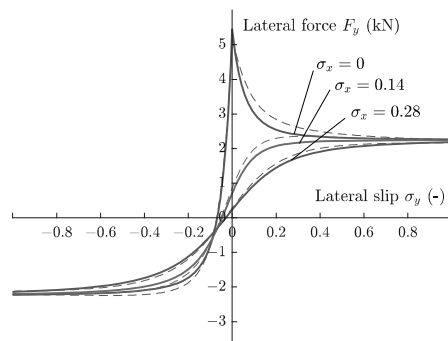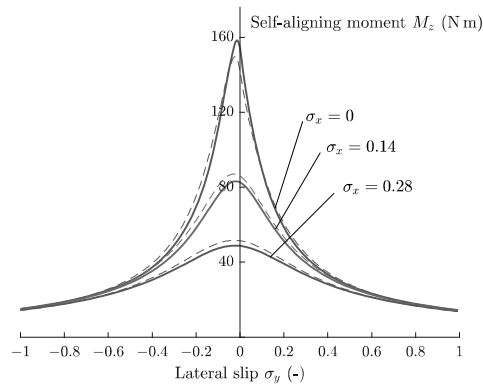
Figure 1. Steady-state characteristics predicted by the classic (solid lines) and exact (dashed lines) LuGre-brush theories for different values of the translational slips σ_x and σ_y for a rectangular contact patch. Tyre parameters: $\varphi = 3.33$ m^{-1}, $\chi_\gamma = 0.9$, $F_z = 3000$ N, $a = 0.075$ m, $b = 0.05$ m, $\mu_s = 1$, $\mu_d = 0.7$. (a) Longitudinal force F_x versus longitudinal slip σ_x, (b) lateral force F_y versus lateral slip σ_y, (c) self-aligning moment M_z versus lateral slip σ_y.
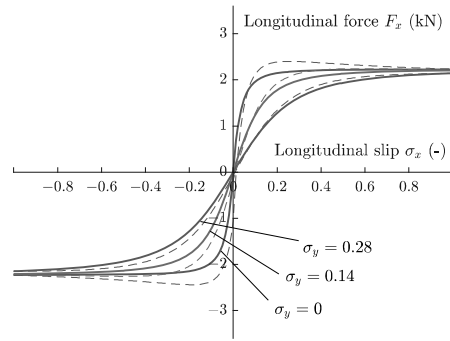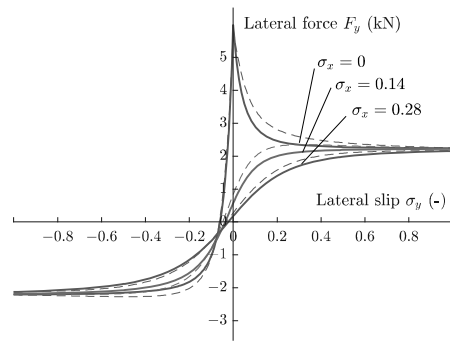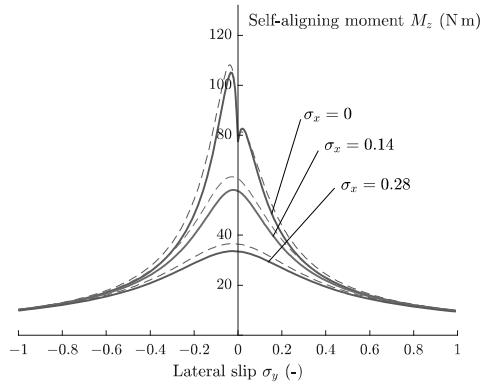
Figure 2. Steady-state characteristics predicted by the classic (solid lines) and exact (dashed-lines) LuGre-brush theories for different values of the translational slips σ_x and σ_y for an elliptical contact patch. Tyre parameters: $\varphi = 3.33\,\mathrm{m}^{-1}$, $\chi_\gamma = 0.9$, $F_z = 3000$ N, $a = 0.075$ m, $b = 0.05$ m, $\mu_\mathrm{s} = 1$, $\mu_\mathrm{d} = 0.7$. (a) Longitudinal force F_x versus longitudinal slip σ_x, (b) lateral force F_y versus lateral slip σ_y, (c) self-aligning moment M_z versus lateral slip σ_y.
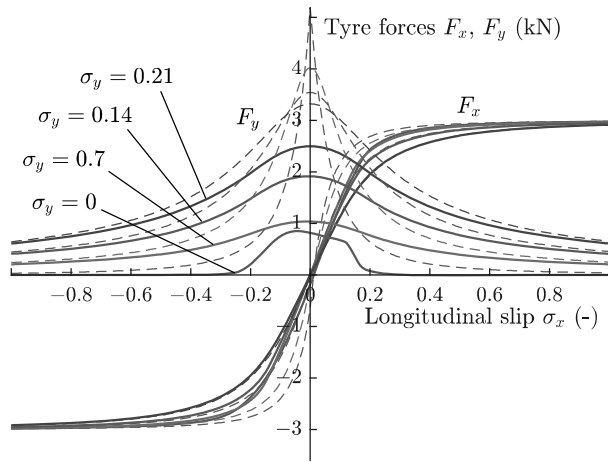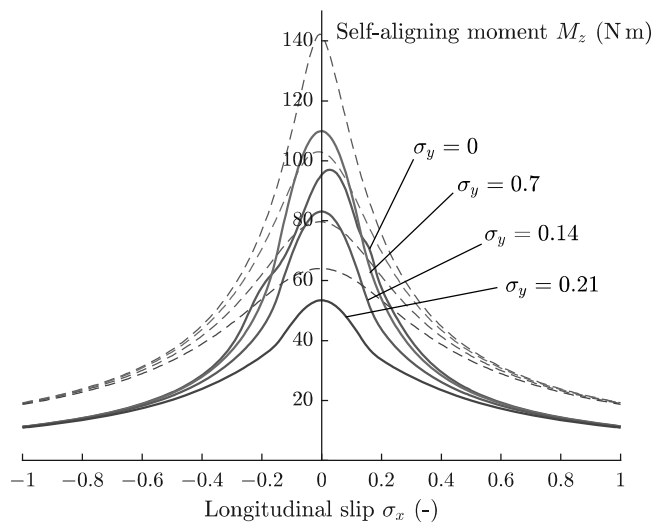
(a)

(b)

Figure 3. Steady-state characteristics predicted by the exact brush (solid lines) and LuGre-brush (dashed lines) tyre models for different values of the translational slips σ_x and σ_y for a rectangular contact patch. Tyre parameters: $\varphi = 3.33\,\mathrm{m}^{-1}$, $\chi_\gamma = 0.9$, $F_z = 3000\,\mathrm{N}$, $a = 0.075\,\mathrm{m}$, $b = 0.05\,\mathrm{m}$, $\mu_\mathrm{s} \equiv \mu_\mathrm{d} = 1$. (a) Tyre forces F_x, F_y versus longitudinal slip σ_x and (b) self-aligning moment M_z versus longitudinal slip σ_x.

the magnitude of the total tangential force can never exceed the friction limit $\mu_\mathrm{s} F_z$. This is not necessarily true in the LuGre-brush theory, which might yield relatively large values for the frictional state $\boldsymbol{z}^-(\boldsymbol{x})^4$. As a result, in the example of Figure 3(a), the combined effect of the translational slip $\boldsymbol{\sigma}$ and spin φ generates a lateral force F_y that in some cases is even higher than the vertical load F_z acting upon the tyre. The less pronounced mismatch

between the two trends for the self-aligning moment in Figure 3(b) may be explained using a similar rationale.

Analogous considerations also hold for the case of an elliptical contact patch, which is not discussed in this paper for brevity.

5. Aggregate model for tyre forces and moment

The exact formulation of the LuGre-brush tyre model developed in Section 3 represents the tyre dynamics in terms of PDEs. For simulation and control purposes, however, it may be beneficial to derive a simplified description based on systems of ordinary differential equations (ODEs). In this context, several contributions may be found in the literature that develop approximated formulations considering the aggregate dynamics of the frictional state $z(x, t)$. Following the approaches outlined in [51–57], the present section extends this class of models to account for large camber angles and two-dimensional contact geometries.

The analysis is conducted under the following Assumption 5.1.

Assumption 5.1: *The vertical pressure distribution $q_z \in C^1(\mathscr{P}; \mathbb{R})$ vanishes on the trailing edge, i.e. $q_z(x) = 0$ for $x \in \mathscr{T}$.*

5.1. Aggregate model for tyre force

The time-varying tyre forces may be described in terms of an aggregate state, which may be interpreted as an average tangential stress acting inside the contact patch. In this context, it is customary to define

$$\hat{z}(t) \triangleq \frac{1}{F_z} \iint_{\mathscr{P}} z(x, t) q_z(x) \, dx, \tag{36}$$

so that Equation (13a) may be restated as

$$F_t(t) = F_z \Big(\mathbf{C}_0(t) + V_r(t) \mathbf{C}_2 \mathbf{A}_{\varphi_\psi}(t) \Big) \hat{z}(t) + F_z \mathbf{C}_1 \dot{\hat{z}}(t)$$

$$+ V_r(t) \mathbf{C}_2 \left(\sigma(t) + \frac{\mathbf{A}_\varphi(t)}{F_z} \iint_{\mathscr{P}} x q_z(x) \, dx \right). \tag{37}$$

Equation (37) should be complemented with another relationship for the dynamics of the aggregate state $\hat{z}(t)$. To this end, differentiating Equation (36) with respect to time gives

$$\dot{\hat{z}}(t) = \frac{1}{F_z} \iint_{\mathscr{P}} \frac{\partial z(x, t)}{\partial t} q_z(x) \, dx$$

$$= V_r(t) \Big(\tilde{\mathbf{A}}_{\varphi_\psi}(t) - \mathbf{K}(t) \Big) \hat{z} + V_r(t) \left(\sigma(t) + \frac{\mathbf{A}_\varphi(t)}{F_z} \iint_{\mathscr{P}} x q_z(x) \, dx \right)$$

$$- \frac{V_r(t)}{F_z} \oint_{\partial \mathscr{P}} z(x, t) q_z(x) \bar{v}_t(x, t) \cdot \hat{v}_{\partial \mathscr{P}}(x) \, dL, \tag{38}$$

where it has been used the fact that the velocity field $\bar{v}_t(x, t)$ is solenoidal, i.e. $\nabla_t \cdot \bar{v}_t(x, t) = 0$. In deriving Equation (38), it should be noticed that the frictional state $z(x, t)$ must always

be continuous on a travelling edge. Discontinuities may only take place on the characteristic lines separating the subdomains of the contact patch where different analytical solutions are obtained depending on the boundary prescription. Therefore, on these lines the boundary terms vanish, as it happens also for the last integral in Equation (38) if Assumption 5.1 is satisfied.

The matrix $\mathbf{K}(t)$ appearing in Equation (38) is diagonal and time-varying:

$$\mathbf{K}(t) = \begin{bmatrix} \kappa_x(t) & 0 \\ 0 & \kappa_y(t) \end{bmatrix}, \tag{39}$$

with the entries $\kappa_x(t)$ and $\kappa_y(t)$ given by

$$\kappa_x(t) \triangleq -\frac{\iint_{\mathscr{P}} z_x(\boldsymbol{x}, t)\big(\bar{\boldsymbol{v}}_t(\boldsymbol{x}, t) \cdot \nabla_t q_z(\boldsymbol{x})\big)\, \mathrm{d}\boldsymbol{x}}{\iint_{\mathscr{P}} z_x(\boldsymbol{x}, t) q_z(\boldsymbol{x})\, \mathrm{d}\boldsymbol{x}},$$

$$\kappa_y(t) \triangleq -\frac{\iint_{\mathscr{P}} z_y(\boldsymbol{x}, t)\big(\bar{\boldsymbol{v}}_t(\boldsymbol{x}, t) \cdot \nabla_t q_z(\boldsymbol{x})\big)\, \mathrm{d}\boldsymbol{x}}{\iint_{\mathscr{P}} z_y(\boldsymbol{x}, t) q_z(\boldsymbol{x})\, \mathrm{d}\boldsymbol{x}}. \tag{40}$$
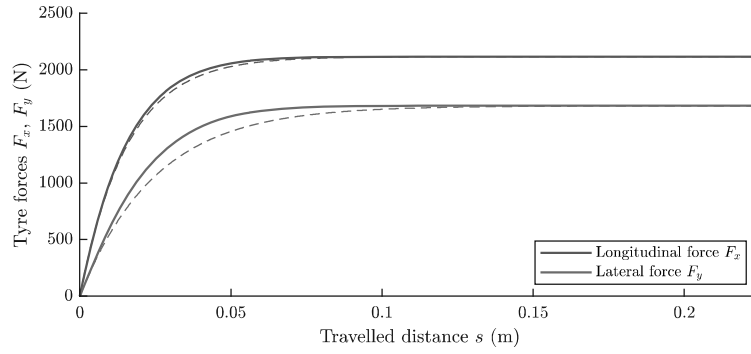
It should be observed that the functions $\kappa_x(t)$ and $\kappa_y(t)$ defined in the above Equation (40) depend upon the frictional state $\boldsymbol{z}(\boldsymbol{x}, t)$, which is however unknown. Different solutions have been proposed in the literature to approximate them. In particular, a common approach consists in replacing the expression for the time-varying frictional state $\boldsymbol{z}(\boldsymbol{x}, t)$ with the corresponding stationary solution $\boldsymbol{z}^-(\boldsymbol{x})$. This guarantees that the lumped model and the original one yield the same result in steady-state conditions. Another option is to postulate *a priori* an analytical function to describe the quantity $\boldsymbol{z}(\boldsymbol{x}, t)$. A more exhaustive discussion may be found in dedicated works [51–57], whereas the present paper privileges the first method for purposes of simplicity.

A comparison between the transient response of the tyre forces to a constant slip input $\boldsymbol{\sigma}$ according to the exact and aggregate formulations is illustrated in Figure 4 for different combinations of σ_x, σ_y and a fixed value of $\varphi = 3.33\ \mathrm{m}^{-1}$ (again with $\chi_\gamma = 0.9$). The evolution of the tyre characteristics is shown versus the travelled distance s instead of the time t (since it is assumed $\mathbf{C}_1 = \mathbf{C}_2 = \mathbf{0}$ for simplicity, the problem is indeed independent of the tyre speed). In general, a very encouraging agreement may be noticed between the two models, especially concerning the longitudinal force. In any case, the trends predicted by the lumped formulation converge to the exact ones approximately within $s = 0.15\ \mathrm{m}$.

5.2. Aggregate model for self-aligning moment

An approximated model for the self-aligning moment with aggregate dynamics may be derived similarly to what done for the tangential forces. In particular, the following states may be defined:

$$\hat{z}_{xx}(t) \triangleq \frac{1}{aF_z} \iint_{\mathscr{P}} x z_x(\boldsymbol{x}, t) q_z(\boldsymbol{x})\, \mathrm{d}\boldsymbol{x}, \quad \hat{z}_{xy}(t) \triangleq \frac{1}{bF_z} \iint_{\mathscr{P}} y z_x(\boldsymbol{x}, t) q_z(\boldsymbol{x})\, \mathrm{d}\boldsymbol{x},$$

$$\hat{z}_{yx}(t) \triangleq \frac{1}{aF_z} \iint_{\mathscr{P}} x z_y(\boldsymbol{x}, t) q_z(\boldsymbol{x})\, \mathrm{d}\boldsymbol{x}, \quad \hat{z}_{yy}(t) \triangleq \frac{1}{bF_z} \iint_{\mathscr{P}} y z_y(\boldsymbol{x}, t) q_z(\boldsymbol{x})\, \mathrm{d}\boldsymbol{x}, \tag{41}$$
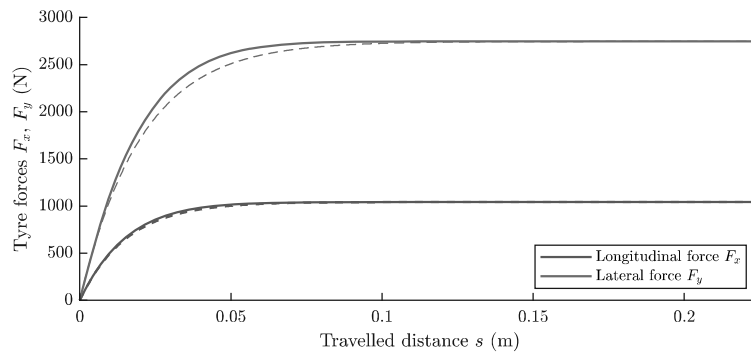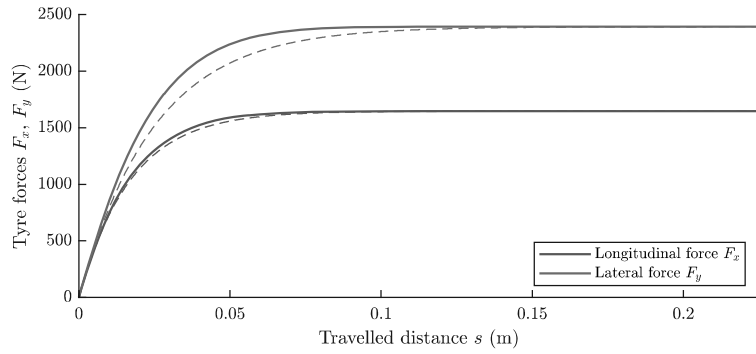
Figure 4. Transient response of the longitudinal and lateral tyre forces F_x, F_y according to the exact LuGre formulation (solid lines) and the lumped model (dashed lines) when subjected to different constant slip inputs. Tyre parameters: $a = 0.075$ m, $b = 0.05$ m, $\mu_s = 1$, $\mu_d = 0.7$, $\delta = 0.6$, $V_r = 10$ m s^{-1}, $v_\delta = 3.49$ m s^{-1}, $c_{0xx} = c_{0yy} = 320$, $c_{0xy} = c_{0yx} = 0$ m^{-1}. (a) Transient response of tyre forces F_x and F_y to constant slip inputs $\sigma_x = 0.14$, $\sigma_y = 0.07$, (b) transient response of tyre forces F_x and F_y to constant slip inputs $\sigma_x = 0.07$, $\sigma_y = 0.14$, (c) transient response of tyre forces F_x and F_y to constant slip inputs $\sigma_x = \sigma_y = 0.1$.

where a and b are two characteristic geometrical parameters in longitudinal and lateral direction, respectively (intuitively, for a symmetrical contact patch, they would correspond to the semilength and semiwidth). It may be easily inferred that the aggregate states in Equation (41) represent moments averaged over the contact patch. Then the dynamic equation for the self-aligning moment becomes

$$
\begin{aligned}
M_z(t) = {} & aF_z\big(c_{0yx} + V_{\mathrm{r}}(t)c_{2yy}\varphi_\psi(t)\big)\hat{z}_{xx}(t) - bF_z\big(c_{0xx} + V_{\mathrm{r}}(t)c_{2xy}\varphi_\psi(t)\big)\hat{z}_{xy}(t) \\
& + aF_z\big(c_{0yy} - V_{\mathrm{r}}(t)c_{2yx}\varphi_\psi(t)\big)\hat{z}_{yx}(t) - bF_z\big(c_{0xy} - V_{\mathrm{r}}(t)c_{2xx}\varphi_\psi(t)\big)\hat{z}_{yy}(t) \\
& + aF_z c_{1yx}\dot{\hat{z}}_{xx}(t) - bF_z c_{1xx}\dot{\hat{z}}_{xy}(t) + aF_z c_{1yy}\dot{\hat{z}}_{yx} - bF_z c_{1xy}\dot{\hat{z}}_{yy} \\
& + \frac{V_{\mathrm{r}}(t)}{abF_z} \iint_{\mathscr{P}} \Big[\sigma_x(t)\big(bc_{2yx}x - ac_{2xx}y\big) + \sigma_y(t)\big(bc_{2yy}x - ac_{2xy}y\big)\Big]q_z(\boldsymbol{x})\,\mathrm{d}\boldsymbol{x} \\
& + \frac{V_{\mathrm{r}}(t)}{abF_z} \iint_{\mathscr{P}} \Big[ac_{2yy}x^2 - \big(ac_{2xy} + bc_{2yx}\big)xy + bc_{2xx}y^2\Big]\varphi(t)q_z(\boldsymbol{x})\,\mathrm{d}\boldsymbol{x}, \quad (42)
\end{aligned}
$$

being the dynamics of the states $\hat{z}_{xx}(t)$, $\hat{z}_{xy}(t)$, $\hat{z}_{yx}(t)$ and $\hat{z}_{yy}(t)$ described by the two following systems of coupled ODEs:

$$
\begin{aligned}
\dot{\hat{z}}_{xx}(t) = {} & -V_{\mathrm{r}}(t)\big(\varphi_{xx}(t) + \kappa_{xx}(t)\big)\hat{z}_{xx}(t) - V_{\mathrm{r}}(t)\big(\varphi_{xy}(t) + \varphi_\psi(t)\big)\hat{z}_{yx}(t) \\
& + \frac{V_{\mathrm{r}}(t)}{aF_z} \iint_{\mathscr{P}} x\big(\sigma_x(t) - \varphi(t)y\big)q_z(\boldsymbol{x})\,\mathrm{d}\boldsymbol{x} \\
& - \frac{V_{\mathrm{r}}(t)}{aF_z} \oint_{\partial\mathscr{P}} z_x(\boldsymbol{x},t)xq_z(\boldsymbol{x})\bar{\boldsymbol{v}}_t(\boldsymbol{x},t)\cdot\hat{\boldsymbol{v}}_{\partial\mathscr{P}}(\boldsymbol{x})\,\mathrm{d}L, \quad (43\mathrm{a})
\end{aligned}
$$

$$
\begin{aligned}
\dot{\hat{z}}_{yx}(t) = {} & -V_{\mathrm{r}}(t)\big(\varphi_{xy}(t) - \varphi_\psi(t)\big)\hat{z}_{xx}(t) - V_{\mathrm{r}}(t)\big(\varphi_{yy}(t) + \kappa_{yx}(t)\big)\hat{z}_{yx}(t) \\
& + \frac{V_{\mathrm{r}}(t)}{aF_z} \iint_{\mathscr{P}} x\big(\sigma_y(t) + \varphi(t)x\big)q_z(\boldsymbol{x})\,\mathrm{d}\boldsymbol{x} \\
& - \frac{V_{\mathrm{r}}(t)}{aF_z} \oint_{\partial\mathscr{P}} z_y(\boldsymbol{x},t)xq_z(\boldsymbol{x})\bar{\boldsymbol{v}}_t(\boldsymbol{x},t)\cdot\hat{\boldsymbol{v}}_{\partial\mathscr{P}}(\boldsymbol{x})\,\mathrm{d}L, \quad (43\mathrm{b})
\end{aligned}
$$

and

$$
\begin{aligned}
\dot{\hat{z}}_{xy}(t) = {} & -V_{\mathrm{r}}(t)\big(\varphi_{xx}(t) + \kappa_{xy}(t)\big)\hat{z}_{xy}(t) - V_{\mathrm{r}}(t)\big(\varphi_{xy}(t) + \varphi_\psi(t)\big)\hat{z}_{yy}(t) \\
& + \frac{V_{\mathrm{r}}(t)}{bF_z} \iint_{\mathscr{P}} y\big(\sigma_x(t) - \varphi(t)y\big)q_z(\boldsymbol{x})\,\mathrm{d}\boldsymbol{x} \\
& - \frac{V_{\mathrm{r}}(t)}{bF_z} \oint_{\partial\mathscr{P}} z_x(\boldsymbol{x},t)yq_z(\boldsymbol{x})\bar{\boldsymbol{v}}_t(\boldsymbol{x},t)\cdot\hat{\boldsymbol{v}}_{\partial\mathscr{P}}(\boldsymbol{x})\,\mathrm{d}L, \quad (44\mathrm{a})
\end{aligned}
$$

$$
\begin{aligned}
\dot{\hat{z}}_{yy}(t) = {} & -V_{\mathrm{r}}(t)\big(\varphi_{yx}(t) - \varphi_\psi(t)\big)\hat{z}_{xy}(t) - V_{\mathrm{r}}(t)\big(\varphi_{yy}(t) + \kappa_{yy}(t)\big)\hat{z}_{yy}(t) \\
& + \frac{V_{\mathrm{r}}(t)}{bF_z} \iint_{\mathscr{P}} y\big(\sigma_y(t) + \varphi(t)x\big)q_z(\boldsymbol{x})\,\mathrm{d}\boldsymbol{x} \\
& - \frac{V_{\mathrm{r}}(t)}{bF_z} \oint_{\partial\mathscr{P}} z_y(\boldsymbol{x},t)yq_z(\boldsymbol{x})\bar{\boldsymbol{v}}_t(\boldsymbol{x},t)\cdot\hat{\boldsymbol{v}}_{\partial\mathscr{P}}(\boldsymbol{x})\,\mathrm{d}L. \quad (44\mathrm{b})
\end{aligned}
$$

Once again, it is worth noticing that the boundary terms in Equations (43a) and (44a) vanish if Assumption 5.1 is satisfied.
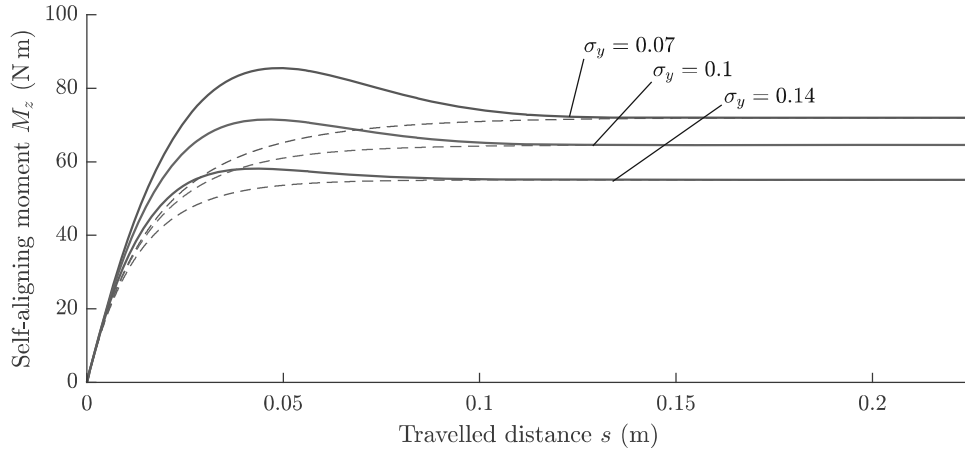
Figure 5. Transient response of the self-aligning moment M_z according to the exact LuGre formulation (solid lines) and the lumped model (dashed lines) when subjected to different constant lateral slip inputs. Tyre parameters: $a = 0.075\,\text{m}, b = 0.05\,\text{m}, \mu_s = 1, \mu_d = 0.7, \delta = 0.6, V_r = 10\,\text{m s}^{-1}, v_\delta = 3.49\,\text{m s}^{-1}, c_{0xx} = c_{0yy} = 320, c_{0xy} = c_{0yx} = 0\,\text{m}^{-1}$.

The functions $\kappa_{xx}(t)$, $\kappa_{xy}(t)$, $\kappa_{yx}(t)$ and $\kappa_{yy}(t)$ appearing in Equations (43a) and (44a) read

$$\kappa_{xx}(t) \triangleq -\frac{\iint_{\mathscr{P}} z_x\left(\bar{\boldsymbol{v}}_t(\boldsymbol{x}, t) \cdot \nabla_t x q_z(\boldsymbol{x})\right) \mathrm{d}\boldsymbol{x}}{\iint_{\mathscr{P}} x z_x(\boldsymbol{x}, t) q_z(\boldsymbol{x}) \mathrm{d}\boldsymbol{x}}, \quad \kappa_{xy}(t) \triangleq -\frac{\iint_{\mathscr{P}} z_x\left(\bar{\boldsymbol{v}}_t(\boldsymbol{x}, t) \cdot \nabla_t y q_z(\boldsymbol{x})\right) \mathrm{d}\boldsymbol{x}}{\iint_{\mathscr{P}} y z_x(\boldsymbol{x}, t) q_z(\boldsymbol{x}) \mathrm{d}\boldsymbol{x}},$$

$$\kappa_{yx}(t) \triangleq -\frac{\iint_{\mathscr{P}} z_y\left(\bar{\boldsymbol{v}}_t(\boldsymbol{x}, t) \cdot \nabla_t x q_z(\boldsymbol{x})\right) \mathrm{d}\boldsymbol{x}}{\iint_{\mathscr{P}} x z_y(\boldsymbol{x}, t) q_z(\boldsymbol{x}) \mathrm{d}\boldsymbol{x}}, \quad \kappa_{yy}(t) \triangleq -\frac{\iint_{\mathscr{P}} z_y\left(\bar{\boldsymbol{v}}_t(\boldsymbol{x}, t) \cdot \nabla_t y q_z(\boldsymbol{x})\right) \mathrm{d}\boldsymbol{x}}{\iint_{\mathscr{P}} y z_y(\boldsymbol{x}, t) q_z(\boldsymbol{x}) \mathrm{d}\boldsymbol{x}},$$

$$(45)$$

and may be again approximated using the steady-state solution $\boldsymbol{z}^-(\boldsymbol{x})$ in place of the general expressions for $\boldsymbol{z}(\boldsymbol{x}, t)$.

As already done for the longitudinal and lateral tyre characteristics, some possible transient evolutions of the self-aligning moment according to both the exact and lumped formulations are shown in Figure 5 for different lateral slip inputs σ_y and a fixed spin $\varphi = 3.33\,\text{m}^{-1}$. In this case, the response from the aggregate dynamic equations converges still relatively fast to that of the exact formulation, but the discrepancy between the two models is more evident. In particular, whilst the exact formulation predicts a transient peak, the lumped model does not. This should however be expected, since the aggregate formulation consists of two linear systems [79,80].

6. Conclusion

This paper presented an extended version of the LuGre-brush tyre model to handle large camber angles and turning speeds. In this context, the first main contribution of the manuscript consisted of the analytical derivation of the steady-state and transient solutions for the frictional state variable when considering constant slip inputs. Specifically, closed-form solutions were deduced for a rectangular and elliptical contact patch by resorting to

classic results for the theory of linear PDEs. A comparison against the standard version of the LuGre-brush tyre model highlighted minor discrepancies between the steady-state tyre characteristics predicted by the refined theory and the standard one. A possible explanation to this may be sought in that, in order to derive closed-form solutions, in this paper, the nonlinear terms involving the sliding velocity were approximated not only by neglecting the contribution due to the internal frictional state but also the variability with the coordinate inside the contact patch. In this context, a possible extension, which would however require numerical methods for hyperbolic systems of PDEs [82], could be to also taken into account the dependence upon the space variables.

On the other hand, significant differences could be observed when comparing the LuGre-brush theory for large camber angles to the exact formulation of the brush models presented in [58,59], especially at low values of the longitudinal slip. The enhanced, physical model presented in this paper may thus have the potential to become a viable alternative to Pacejka's MF, which currently appears to be the only analytical model capable of dealing effectively with large camber angles and steering speeds.

In the second part of the manuscript, approximated models for the transient tangential forces and moment were developed based on the aggregate dynamics of averaged frictional states over the contact patch. This approach is well established in the literature and leads to the derivation of simplified models describing the time-varying tyre characteristics using linear systems of ODEs. As opposed to PDEs, linear dynamical systems of ODEs are in fact easier to implement when it comes to control applications and vehicle dynamics studies. The transient response of the tyre forces and moment predicted using the aggregate model was validated against the exact formulation in terms of PDEs, showing an encouragingly good agreement.

A major disadvantage of the extended formulation presented in the paper is that, owing to the complexity of the analytical solutions, some functions that play a fundamental role in the derivation of the approximated models need to be evaluated numerically. Therefore, future research efforts should be devoted to building look-up tables for these functions depending on different tyre structural parameters and operating conditions. The validation of the model should also be conducted to assess its ability to correctly replicate the steady-state tyre characteristics at large spin slips. This will require *ad-hoc* experiments or procedures [46], as well as a more detailed model for the contact patch shape as a function of the camber angle. In this context, it would be also interesting to perform a comparison against the forces and moment predicted using a full version of Pacejka's MF.

Nomenclature

Forces and moments	Unit	Description
F_t	N	Tangential tyre force vector
F_x, F_y	N	Longitudinal and lateral tyre forces
M_z	N m	Self-aligning moment
q_z	$N\,m^{-2}$	Vertical pressure
z	m	Internal frictional state vector
z_x, z_y	m	Longitudinal and lateral frictional states

(*continued*)

z^-	m	Steady-state frictional state vector
z_x^-, z_y^-	m	Steady-state longitudinal and lateral frictional states
z^+	m	Transient frictional state vector
z_x^+, z_y^+	m	Transient longitudinal and lateral frictional states
$\hat{z}$	m	Aggregate internal frictional state vector for tyre forces
$\hat{z}_x, \hat{z}_y$	m	Aggregate longitudinal and lateral frictional states for tyre forces
$\hat{z}_{xx}, \hat{z}_{yy}$	m	Aggregate diagonal frictional states for self-aligning moment
$\hat{z}_{xy}, \hat{z}_{yx}$	m	Aggregate diagonal frictional states for self-aligning moment

Coordinates	Unit	Description
s	m	Travelled distance
t	s	Time
x	m	Coordinate vector
x, y, z	m	Longitudinal, lateral and vertical coordinates
x_0	m	Initial data vector (ID)
x_0, y_0	m	Initial longitudinal and lateral data (ID)
ξ	m	Local coordinate vector
ξ, η	m	Alternative longitudinal and lateral coordinates

Speeds	Unit	Description
v_t	m s^{-1}	Tangential velocity field
v_x, v_y	m s^{-1}	Longitudinal and lateral components of the tangential velocity field
$\bar{v}_t$	–	Nondimensional tangential velocity field
$\bar{v}_x, \bar{v}_y$	–	Longitudinal and lateral components of the nondimensional velocity field
v_δ	m s^{-1}	Stribeck velocity
v_μ	m s^{-1}	Micro-sliding velocity
v_μ	m s^{-1}	Total micro-sliding speed
$\hat{v}_\mu$	–	Average micro-sliding speed
$v_{\mu x}, v_{\mu y}$	m s^{-1}	Longitudinal and lateral micro-sliding speeds
V_r	m s^{-1}	Tyre rolling speed
$\dot{\psi}$	rad s^{-1}	Steering speed

Slip parameters	Unit	Description
χ_γ, χ_ψ	–	Camber and turn ratio
ε_γ	–	Camber reduction factor
σ	–	Theoretical translational slip vector
σ	–	Total theoretical translational slip
σ_x, σ_y	–	Theoretical longitudinal and lateral slip
φ	m^{-1}	Rotational slip or spin parameter
$\varphi_\gamma, \varphi_\psi$	m^{-1}	Camber and turn spin parameters

Rotational matrices and tensors	Unit	Description
$\mathbf{A}_\varphi, \mathbf{A}_{\varphi_\gamma}, \mathbf{A}_{\varphi_\psi}$	m^{-1}	Spin, camber spin and turn spin tensors
$\tilde{\mathbf{A}}_{\varphi_\psi}$	m^{-1}	Modified turn spin tensor
$\varphi_{xx}, \varphi_{yy}$	m^{-1}	Diagonal elements in the modified turn spin tensor
$\varphi_{xy}, \varphi_{yx}$	m^{-1}	Cross elements in the modified turn spin tensor
$\mathbf{R}_{\varphi_\gamma}$	–	Camber spin rotation matrix
$\tilde{\Phi}_{\varphi_\psi}$	–	Modified transition matrix for turn spin

Geometric parameters	Unit	Description
a, b	m	Contact patch semilength and semiwidth
x_{C_γ}, x_{C_ψ}	m	Cambering centre and turning centre coordinate vectors
$x_{\mathscr{L}}$	m	Leading edge explicit representation
$x_{\mathscr{N}}$	m	Neutral edge explicit representation
y_{C_γ}, y_{C_ψ}	m	Cambering centre and turning centre lateral coordinates
$y_{\mathscr{L}}$	m	Leading edge explicit representation
$y_{\mathscr{N}}$	m	Neutral edge explicit representation
R_r	m	Rolling radius
R_γ, R_ψ	m	Cambering radius and turning radius

γ	rad	Camber angle
λ_x, λ_y	m	Longitudinal and lateral relaxation lengths

Curvature matrices	Unit	Description
$\mathbf{C}_0$	m^{-1}	Zeroth-order frictional matrix
c_{0xx}, c_{0yy}	m^{-1}	Diagonal entries of the zeroth-order frictional matrix
c_{0xy}, c_{0yx}	m^{-1}	Cross entries of the zeroth-order frictional matrix
$\mathbf{C}_1$	$s\,m^{-1}$	First-order frictional matrix
c_{1xx}, c_{1yy}	$s\,m^{-1}$	Diagonal entries of the first-order frictional matrix
c_{1xy}, c_{1yx}	$s\,m^{-1}$	Cross entries of the first-order frictional matrix
$\mathbf{C}_2$	$s\,m^{-1}$	First-order frictional matrix
c_{2xx}, c_{2yy}	$s\,m^{-1}$	Diagonal entries of the first-order frictional matrix
c_{2xy}, c_{2yx}	$s\,m^{-1}$	Cross entries of the first-order frictional matrix
$\mathbf{K}$	m^{-1}	Curvature functions matrix for aggregate model for tyre forces
k_x, k_y	m^{-1}	Diagonal curvature functions matrix for tyre forces
k_{xx}, k_{yy}	m^{-1}	Diagonal curvature functions for self-aligning moment
k_{xy}, k_{yx}	m^{-1}	Cross curvature functions for self-aligning moment

Frictional parameters	Unit	Description
$\boldsymbol{\mu}$	–	Friction coefficient vector
μ_x, μ_y	–	Longitudinal and lateral friction coefficients
μ_d	–	Dynamic friction coefficient
μ_s	–	Static friction coefficient

Functions and operators	Unit	Description
∇_t	m^{-1}	Tangential gradient
$\Gamma(\cdot)$	m^2	Gamma function
$\Sigma(\cdot)$	m	Sigma function
$\boldsymbol{\Psi}(\cdot)$	m	Vector-valued psi function
$\Psi_x(\cdot), \Psi_y(\cdot)$	m	Longitudinal and lateral psi functions

Sets	Unit	Description
$\mathscr{P}$	m^2	Contact patch
$\mathscr{P}^-$	m^2	Steady-state zone
$\mathscr{P}^+$	m^2	Transient zone
$\mathring{\mathscr{P}}$	m^2	Interior of $\mathscr{P}$
$\partial\mathscr{P}$	m	Boundary of $\mathscr{P}$
$\mathscr{L}$	m	Leading edge
$\mathscr{N}$	m	Neutral edge
$\mathscr{S}$	m	Sliding edge
$\mathscr{T}$	m	Trailing edge
$\mathbb{R}_{\geq 0}$	–	Set of positive real numbers (including 0)
$\mathbb{R}_{>0}$	–	Set of strictly positive real numbers (excluding 0)

Implicit curves	Unit	Description
γ_Σ	m	Implicit representation of the travelling edge

Notes

1. It should be clarified that, in reality, the sliding velocity should also account for the term $\dfrac{d\boldsymbol{z}(\boldsymbol{x}, t)}{dt} = \dfrac{\partial \boldsymbol{z}(\boldsymbol{x}, t)}{\partial t} + (\boldsymbol{v}_t(\boldsymbol{x}, t) \cdot \nabla_t)\boldsymbol{z}(\boldsymbol{x}, t)$ if the variable $\boldsymbol{z}(\boldsymbol{x}, t)$ is interpreted as a real deflection. In the brush models, such a sliding velocity is denoted by $\boldsymbol{v}_s(\boldsymbol{x}, t) = \dfrac{d\boldsymbol{z}(\boldsymbol{x}, t)}{dt} + \boldsymbol{v}_\mu(\boldsymbol{x}, t)$.

2. For an isotropic tyre, straightforward calculations yield $c_{0xx} = c_{0yy} = 4kab/F_z$, where k is the bristle stiffness according to the exact brush theory.

3. In this regard, it is important to clarify that the term related to the partial derivatives of the bristle deflection was neglected in the calculation of the direction for the shear stress acting inside the sliding zone of the contact patch. This is usually a reasonable approximation [1].

4. In this context, however, it is worth observing that the problem described by the linear PDEs (8) with BC (9a) fulfils the noncharacteristic condition [59], and therefore the steady-state solution $z^-(x)$ for the internal frictional state should not be expected to diverge for any $x \in \mathscr{P}$. Further details on the purely mathematical aspects may be found in [76,77].

Acknowledgments

Disclosure statement

No potential conflict of interest was reported by the author(s).

ORCID

Luigi Romano http://orcid.org/0000-0001-8435-7696
Bengt Jacobson http://orcid.org/0000-0002-5798-5651

References

[1] Pacejka HB. Tire and vehicle dynamics. 3rd ed. Amsterdam: Elsevier/BH; 2012.

[2] Guiggiani M. The science of vehicle dynamics. 2nd ed. Cham: Springer International; 2018.

[3] Genovese A, Garofano D, Sakhnevych A, et al. Static and dynamic analysis of non-pneumatic tires based on experimental and numerical methods. Appl Sci. 2021;11(23):11–232.

[4] Romano L, Bruzelius F, Jacobson B. Unsteady-state brush theory. Vehicle Syst Dyn. 2021;59(11):1643–1671. https://doi.org/10.1080/00423114.2020.1774625.

[5] Carputo F, D'Andrea D, Risitano G, et al. A neural-network-based methodology for the evaluation of the center of gravity of a motorcycle rider. Vehicles. 2021;3(3):377–389.

[6] Jaiswal M, Mavros G, Rahnejat H, et al. Influence of tyre transience on anti-lock braking. Proc Inst Mechan Eng K J Multi-body Dynam. 2010;224(1):1–17. https://doi.org/10.1243/14644193 JMBD225.

[7] Joa E, Yi K, Hyun Y. Estimation of the tire slip angle under various road conditions without tire–road information for vehicle stability control. Control Eng Pract. 2019;86:129–143. https://doi.org/10.1016/j.conengprac.2019.03.005.

[8] Limebeer DJN, Massaro M. Dynamics and optimal control of road vehicle. Croydon: Oxford University Press; 2018.

[9] O'Neill A, Gruber P, Watts JF, et al. Predicting tyre behaviour on different road surfaces. In: Klomp M, Bruzelius F, Nielsen J, Hillemyr A. editors. Advances in dynamics of vehicles on roads and tracks. IAVSD 2019. Cham: Springer. (Lecture Notes in Mechanical Engineering). Available from: https://doi.org/10.1007/978-3-030-38077-9_215.

[10] O'Neill A, Prins J, Watts JF, et al. Enhancing brush tyre model accuracy through friction measurements. Vehicle Syst Dyn. 2021:1–23. https://doi.org/10.1080/00423114.2021.1893766.

[11] Salehi M, Noordermeer JWM, Reuvekamp LAEM, et al. A new Horizon for evaluating tire grip within a laboratory environment. Tribol Lett. 2020;68:37. https://doi.org/10.1007/s11249-020-1273-5.

[12] Salehi M, Noordermeer JWM, Reuvekamp LAEM, et al. Understanding test modalities of tire grip and laboratory-road correlations with modeling. Tribol Lett. 2021;69:116. https://doi.org/10.1007/s11249-021-01490-2.

[13] von Schlippe B, Dietrich R. Das flattern eined bepneuten rades. Bericht 140 der Lilienthal Gesellschaft. 1941: NACA TM 1365.

[14] Segel L. Force and moment response of pneumatic tires to lateral motion inputs. Trans ASME J Eng Industry. 1966;88:37–44.

[15] Gafvert M, Svendenius J. A novel semi-empirical tyre model for combined slips. Vehicle Syst Dyn. 2005;43(5):351–384.

[16] Bai F, Guo K, Lu D. Tire model for turn slip properties. SAE Int J Commer Vehicles. 2013;6(2):353–361.

[17] Xu N, Guo K, Zhang X, et al. An analytical tire model with flexible carcass for combined slips. Math Problems Eng. 2014;2014:397–538.

[18] Takács D, Orosz G, Stépán G. Delay effects in shimmy dynamics of wheels with stretched string-like tyres. Eur J Mechan A/Solids. 2009;28(3):516–525.

[19] Takács D, Stépán G. Micro-shimmy of towed structures in experimentally uncharted unstable parameter domain. Vehicle Syst Dyn. 2012;50(11):1613–1630.

[20] Takács D, Stépán G, Hogan SJ. Isolated large amplitude periodic motions of towed rigid wheels. Nonlinear Dyn. 2008;52:27–34. https://doi.org/10.1007/s11071-007-9253-y.

[21] Takács D, Stépán G. Experiments on quasiperiodic wheel shimmy. ASME J Comput Nonlinear Dyn. 2009;4(3):031007. https://doi.org/10.1115/1.3124786.

[22] Takács D, Stépán G. Contact patch memory of tyres leading to lateral vibrations of four-wheeled vehicles. Phil Trans R Soc A. 2013;371:20120427. http://doi.org/10.1098/rsta.2012.0427.

[23] Beregi S, Takács D, Stépán G. Tyre induced vibrations of the car–trailer system. J Sound Vib. 2016;362:214–227.

[24] Beregi S, Takács D, Hos C. Nonlinear analysis of a shimmying wheel with contact-force characteristics featuring higher-order discontinuities. Nonlinear Dyn. 2017;90:877–888. https://doi.org/10.1007/s11071-017-3699-3.

[25] Beregi S, Takacs D, Gyebroszki G, et al. Theoretical and experimental study on the nonlinear dynamics of wheel-shimmy. Nonlinear Dyn. 2019;98:2581–2593. https://doi.org/10.1007/s11071-019-05225-w.

[26] Beregi S, Takacs D, Stepan G. Bifurcation analysis of wheel shimmy with non-smooth effects and time delay in the tyre–ground contact. Nonlinear Dyn. 2019;98:841–858. https://doi.org/10.1007/s11071-019-05123-1.

[27] Beregi S, Takács D. Analysis of the tyre–road interaction with a non-smooth delayed contact model. Multibody Syst Dyn. 2019;45:185–201. https://doi.org/10.1007/s11044-018-09636-2.

[28] Duvaut G, Lions JL. Inequalities in mechanics and physics. Springer-Verlag: Berlin Heidelberg; 1976.

[29] Kalker JJ. Variational principles of contact elastostatics. J Inst Math Appl. 1997;20:199–219.

[30] Persson BNJ. Theory of rubber friction and contact mechanics. J Chem Phys. 2001;115(8):3840–3861. https://doi.org/10.1063/1.1388626.

[31] Persson BNJ, Albohr O, Tartaglino U, et al. On the nature of surface roughness with application to contact mechanics, sealing, rubber friction and adhesion. J Phys Condens Matter. 2004;17(1):R1–R62.

[32] Persson BNJ. Contact mechanics for randomly rough surfaces. Surface Sci Rep. 2006;61(4):201–227. https://doi.org/10.1016/j.surfrep.2006.04.001.

[33] Heinrich G, Klüppel M. Rubber friction, tread deformation and tire traction. Wear. 2008;265(7-8):1052–1060. https://www.sciencedirect.com/science/article/pii/S0043164808000847.

[34] Sakhnevych A. Multiphysical MF-based tyre modelling and parametrisation for vehicle setup and control strategies optimisation. Vehicle Syst Dyn. 2021:1–22. https://www.tandfonline.com/doi/full/10.1080/00423114.2021.1977833.

[35] Higuchi A. Transient response of tyres at large wheel slip and camber [dissertation]. Delft; 1997.

[36] Higuchi A, Pacejka HB. The relaxation length concept at large wheel slip and camber. Vehicle Syst Dyn. 1997;25(1):50–64. https://doi.org/10.1080/00423119708969644.

[37] Pauwelussen JP. The local contact between tyre and road under steady state combined slip conditions. Vehicle Syst Dyn. 2004;41(1):1–26. http://doi.org/10.1076/vesd.41.1.1.23406.

[38] Svendenius J, Wittenmark B. Brush tire model with increased flexibility. In: European Control Conference, Cambridge, UK; 2015. Available from: https://dx.doi.org/10.23919/ECC.2003.7085237.

[39] Svendenius J. Tire modelling and friction estimation [dissertation]. Lund; 2007.

[40] Svendenius J, Gäfvert M, Bruzelius F, et al. Experimental validation of the brush tire model. Tire Sci Technol. 2009;37(2):122–137.

[41] Rill G. Sophisticated but quite simple contact calculation for handling tire models. Multibody Syst Dyn. 2019;45:131–153. https://doi.org/10.1007/s11044-018-9629-4.

[42] Rill G. Road vehicle dynamics: fundamentals and modeling with MATLAB®. 2nd ed. Boca Raton: CRC Press; 2020.

[43] Shaju A, Pandey AK. Modelling transient response using PAC 2002-based tyre model. Vehicle Syst Dyn. 2020;60:20–46. https://doi.org/10.1080/00423114.2020.1802048.

[44] Pacejka HB, Besselink IJM. Magic formula tyre model with transient properties. Vehicle Syst Dyn. 1997;27(1):234–249. https://doi.org/10.1080/00423119708969658.

[45] Besselink IJM, Schmeitz AJC, Pacejka HB. An improved magic formula/swift tyre model that can handle inflation pressure changes. Vehicle Syst Dyn. 2010;48(1):337–352. https://doi.org/10.1080/00423111003748088.

[46] Farroni F. T.R.I.C.K.-Tire/road interaction characterization & knowledge – a tool for the evaluation of tire and vehicle performances in outdoor test sessions. Mech Syst Signal Process. 2016;72-73:808–831. https://doi.org/10.1016/j.ymssp.2015.11.019.

[47] Farroni F, Sakhnevych A, Timpone F. Physical modelling of tire wear for the analysis of the influence of thermal and frictional effects on vehicle performance. Proc Inst Mechan Eng L J Mater Design Appl2017;231(1-2):151–161. https://doi.org/10.1177/1464420716666107.

[48] Romano L, Bruzelius F, Hjort M, et al. Development and analysis of the two-regime transient tyre model for combined slip. Vehicle Syst Dyn. 2022.

[49] Marques F, Flores P, Pimenta Claro JC, et al. A survey and comparison of several friction force models for dynamic analysis of multibody mechanical systems. Nonlinear Dyn. 2016;86:1407–1443. https://doi.org/10.1007/s11071-016-2999-3.

[50] Canudas de Wit C, Olsson H, Astrom KJ, et al. A new model for control of systems with friction. IEEE Trans Automatic Control. 1995;40(3):419–425. https://. doi: 10.1109/9.376053.

[51] Canudas-de-Wit C, Tsiotras P, Velenis E, et al. Dynamic friction models for road/tire longitudinal interaction. Vehicle Syst Dyn. 2003;39(3):189–226. https://doi.org/10.1076/vesd.39.3.189.14152.

[52] Tsiotras P, Velenis E, Sorine M. A LuGre tire friction model with exact aggregate dynamics. Vehicle Syst Dyn. 2004;42(3):195–210. https://doi.org/10.1080/00423110412331289835.

[53] Velenis E, Tsiotras P, Canudas-de-Wit C, et al. Dynamic tyre friction models for combined longitudinal and lateral vehicle motion. Vehicle Syst Dyn. 2005;43(1):3–29. https://doi.org/10.1080/00423110412331290464.

[54] Deur J. Modeling and analysis of longitudinal tire dynamics based on the lugre friction model. IFAC Proc Volumes. 2001;34(1):91–96. https://doi.org/10.1016/S1474-6670(17)34383-5.

[55] Deur J, Asgari J, Hrovat D. A dynamic tire friction model for combined longitudinal and lateral motion. In: Proceedings of the ASME-IMECE World Conference; 2001.

[56] Deur J, Asgari J, Hrovat D. A 3D brush-type dynamic tire friction model. Vehicle Syst Dyn. 2004;42(3):133–173. https://doi.org/10.1080/00423110412331282887.

[57] Deur J, Ivanovic V, Troulis M, et al. Extensions of the LuGre tyre friction model related to variable slip speed along the contact patch length. Int J Vehicle Syst Dyn. 2005;43:508–524. https://doi.org/10.1080/00423110500229808.

[58] Romano L, Bruzelius F, Jacobson B. Brush tyre models for large camber angles and steering speeds. Int J Vehicle Syst Dyn. 2022;60(4):1341–1392. https://doi.org/10.1080/00423114.2020.1854320.

[59] Romano L, Timpone F, Bruzelius F, et al. Analytical results in transient brush tyre models: theory for large camber angles and classic solutions with limited friction. Meccanica. 2022;57:165–191. https://dx.doi.org/10.1007/s11012-021-01422-3.

[60] Romano L. Advanced brush tyre modelling. Cham: Springer; 2022. (Springer Briefs in Applied Sciences).

[61] Krstic M. Boundary control of PDEs: a course on backstepping designs. Philadelphia: SIAM; 2008.

[62] Krstic M. Input-to-state stability for PDEs. Cham: Springer; 2018.
[63] Marques F, Flores P, Claro JCP, et al. Modeling and analysis of friction including rolling effects in multibody dynamics: a review. Multibody Syst Dyn. 2019;45:223–244. https://doi.org/10.1007/s11044-018-09640-6.
[64] Marques F, Wolinski L, Wojtyra M, et al. An investigation of a novel LuGre-based friction force model. Mechan Machine Theory. 2021;166:104493. https://doi.org/10.1016/j.mechmachtheory.2021.104493.
[65] Li J, Zhang Y, Yi J. A hybrid physical-dynamic tire/road friction model. ASME J Dyn Syst Meas Control. 2013 Jan;135(1):011007. https://doi.org/10.1115/1.4006887.
[66] Liang W, Medanic J, Ruhl R. Analytical dynamic tire model. Vehicle Syst Dyn. 2008;46(3):197–227. https://doi.org/10.1080/00423110701267466.
[67] Kikuuwe R. A brush-type tire model with nonsmooth representation. Math Problems Eng. 2019;2019:9747605. https://doi.org/10.1155/2019/9747605.
[68] Kikuuwe R, Takesue N, Sano A, et al. Admittance and impedance representations of friction based on implicit euler integration. IEEE Trans Robot. 2006;22(6):1176–1188. https://doi.org/10.1109/TRO.2006.886262.
[69] Koopman J, Jeltsema D, Verhaegen M. Port-Hamiltonian description and analysis of the LuGre friction model. Simul Model Pract Theory. 2011;19(3):959–968. https://doi.org/10.1016/j.simpat.2010.11.008.
[70] Yu H, Qi Z, Duan J, et al. Multiple model adaptive backstepping control for antilock braking system based on LuGre dynamic tyre model. Int J Vehicle Design. 2015;69(1–4):168–184.
[71] Hou X, Zhang J, Liu W, et al. LuGre model-based longitudinal ride comfort control of vehicle during the post-braking phase. In: 2020 Chinese Automation Congress (CAC); 2020. p. 7307–7313.
[72] Sharifzadeh M, Akbari A, Timpone F, et al. Vehicle tyre/road interaction modeling and identification of its parameters using real-time trust-region methods. IFAC-PapersOnLine. 2016;49(3):111–116. https://doi.org/10.1016/j.ifacol.2016.07.019.
[73] Sharifzadeh M, Timpone F, Farnam A, et al. Tyre-road adherence conditions estimation for intelligent vehicle safety applications. In: Boschetti G, Gasparetto A. editors. Advances in Italian Mechanism Science. Cham: Springer; 2017. (Mechanisms and Machine Science; 47). Available from:https://doi.org/10.1007/978-3-319-48375-7_42.
[74] Sharifzadeh M, Senatore A, Farnam A, et al. A real-time approach to robust identification of tyre–road friction characteristics on mixed-μ roads. Vehicle Syst Dyn. 2019;57(9):1338–136. https://doi.org/10.1080/00423114.2018.1504974.
[75] Pacejka HB. Spin: camber and turning. Vehicle Syst Dyn. 2005;43(1):3–17. https://doi.org/10.1080/00423110500140013.
[76] Evans LC. Partial differential equations. 2nd ed. Providence, Rhode Island: American Mathematical Society; 1996.
[77] Ockendon JR, Howison S, Lacey A, et al. Applied partial differential equations. Oxford: Oxford University Press; 2003.
[78] Polyanin AD, Manzhirov AV. Handbook of mathematics for engineers and scientists. Boca Raton, London: Chapman & Hall/CRC Press; 2007.
[79] Rugh WJ. Linear system theory. 2nd ed. Upper Saddle River: Prentice Hall. Johns Hopkins University; 2007.
[80] Khalil HK. Nonlinear systems. 3rd ed. Upper Saddle River: Prentice Hall; 2002.
[81] Romano L, Timpone F, Bruzelius F, et al. Rolling, tilting and spinning spherical wheels: analytical results using the brush theory. Mechanism Machine Theory. 2022;173:104836. https://doi.org/10.1016/j.mechmachtheory.2022.104836.
[82] Larsson S, Thomee V. Partial differential equations with numerical methods. 1st ed. Berlin, Heidelberg: Springer; 2009.

Appendix 1. Energy estimate for the bristle deflection

This section gives upper bounds on the internal frictional state resulting from the solution of the PDEs (8). For the sake of notation, the time variable t is again replaced by the travelled distance s. The analysis is conducted with respect to the modified formulation described by Equation (8). However, it should be observed that, as opposed to Section 3, the slip inputs and the tangential velocity field are not assumed to be constant over s.

For what follows, it is also beneficial to introduce the notion of L^p-norm $\|\cdot\|_{L^p}$. In particular, consider a domain $\Omega \subseteq \mathbb{R}^2$; then, the L^p-norm $\|\cdot\|_{L^p(\Omega)}$ ($1 \leq p < \infty$) is defined as [76,77]

$$\|\cdot\|_{L^p(\Omega)} \triangleq \left(\iint_\Omega (\cdot)^p \, \mathrm{d}\boldsymbol{x} \right)^{\frac{1}{p}}. \tag{A1}$$

A generic measurable function $f(\cdot)$ is said to belong to the space $L^p(\Omega)$, $1 \leq p < \infty$, denoted $f \in L^p(\Omega)$, if $\|f(\cdot)\|_{L^p(\Omega)} < \infty$. The next Proposition A.1 provides an energy estimate for the L^2-norm $\|z(\cdot, s)\|^2_{L^2(\mathring{\mathscr{P}})}$ of the total internal frictional state $z(\boldsymbol{x}, s) \triangleq \|\boldsymbol{z}(\boldsymbol{x}, s)\|$. In what follows, it is assumed that $z_0(\cdot) \in L^2(\mathring{\mathscr{P}})$ and that all the quantities are sufficiently smooth for the derivation of the result.

Proposition A.1 (Energy estimate for the internal frictional state): *From Equation* (8)*, the following energy estimate holds for the internal frictional state $\boldsymbol{z}(\boldsymbol{x}, s)$:*

$$
\|z(\cdot, s)\|^2_{L^2(\mathring{\mathscr{P}})} \leq \|z_0(\cdot)\|^2_{L^2(\mathring{\mathscr{P}})} \, \mathrm{e}^{\int_0^s \left(1 - \frac{2\hat{v}_\mu(s')}{V_r(s')g\left(\hat{v}_\mu(s')\right)} \lambda_{\min}(\mathbf{C}_0) \right) \mathrm{d}s'}
$$

$$
+ \int_0^s \mathrm{e}^{\int_{s'}^s \left(1 - \frac{2\hat{v}_\mu(\tilde{s})}{V_r(\tilde{s})g\left(\hat{v}_\mu(\tilde{s})\right)} \lambda_{\min}(\mathbf{C}_0) \right) \mathrm{d}\tilde{s}} \left\| \sigma_x(s') - \varphi(s')y \right\|^2_{L^2(\mathring{\mathscr{P}})} \mathrm{d}s'
$$

$$
+ \int_0^s \mathrm{e}^{\int_{s'}^s \left(1 - \frac{2\hat{v}_\mu(\tilde{s})}{V_r(\tilde{s})g\left(\hat{v}_\mu(\tilde{s})\right)} \lambda_{\min}(\mathbf{C}_0) \right) \mathrm{d}\tilde{s}} \left\| \sigma_y(s') + \varphi(s')x \right\|^2_{L^2(\mathring{\mathscr{P}})} \mathrm{d}s', \quad s \in \mathbb{R}_{\geq 0}, \tag{A2}
$$

where $\lambda_{\min}(\mathbf{C}_0)$ is the smallest (positive real) eigenvalue of $\mathbf{C}_0$.

Proof: First, it may be observed that

$$\frac{1}{2} \frac{\partial z^2(\boldsymbol{x}, s)}{\partial s} = \frac{1}{2} \frac{\partial}{\partial s} \|\boldsymbol{z}(\boldsymbol{x}, s)\|^2_2 = z_x(\boldsymbol{x}, s) \frac{\partial z_x(\boldsymbol{x}, s)}{\partial s} + z_y(\boldsymbol{x}, s) \frac{\partial z_y(\boldsymbol{x}, s)}{\partial s}. \tag{A3}$$

Integrating both sides over $\mathring{\mathscr{P}}$ yields, after some manipulations,

$$\frac{1}{2} \frac{\mathrm{d}}{\mathrm{d}s} \|z(\cdot, s)\|^2_{L^2(\mathring{\mathscr{P}})} = \frac{1}{2} \frac{\mathrm{d}}{\mathrm{d}s} \iint_{\mathring{\mathscr{P}}} z^2(\boldsymbol{x}, s) \, \mathrm{d}\boldsymbol{x} = -\frac{1}{2} \iint_{\mathring{\mathscr{P}}} \bar{\boldsymbol{v}}_t(\boldsymbol{x}, s) \cdot \nabla_t z^2(\boldsymbol{x}, s) \, \mathrm{d}\boldsymbol{x}$$

$$+ \iint_{\mathring{\mathscr{P}}} z_x(\boldsymbol{x}, s)\big(\sigma_x(s) - \varphi(s)y\big) + z_y(\boldsymbol{x}, s)\big(\sigma_y(s) + \varphi(s)x\big) \, \mathrm{d}\boldsymbol{x}$$

$$- \frac{\hat{v}_\mu(s)}{V_r(s)g\left(\hat{v}_\mu(s)\right)} \iint_{\mathring{\mathscr{P}}} \boldsymbol{z}(\boldsymbol{x}, s)^{\mathrm{T}} \mathbf{C}_0 \boldsymbol{z}(\boldsymbol{x}, s) \, \mathrm{d}\boldsymbol{x}. \tag{A4}$$

Integrating by parts the first integral term on the right-hand side of Equation (A4) and recalling that $\bar{\boldsymbol{v}}_t(\boldsymbol{x}, s)$ is solenoidal, i.e. $\nabla_t \cdot \bar{\boldsymbol{v}}_t(\boldsymbol{x}, s) = 0$, gives

$$\frac{1}{2} \frac{\mathrm{d}}{\mathrm{d}s} \|z(\cdot, s)\|^2_{L^2(\mathring{\mathscr{P}})} = -\frac{1}{2} \int_{\mathscr{T}} z^2(\boldsymbol{x}, s) \bar{\boldsymbol{v}}_t(\boldsymbol{x}, s) \cdot \hat{\boldsymbol{v}}_{\partial \mathscr{P}}(\boldsymbol{x}) \, \mathrm{d}L$$

$$+ \iint_{\mathring{\mathscr{P}}} z_x(\boldsymbol{x}, s)\big(\sigma_x(s) - \varphi(s)y\big) + z_y(\boldsymbol{x}, s)(\sigma_y(s) + \varphi(s)x) \, \mathrm{d}\boldsymbol{x}$$

$$- \frac{\hat{v}_\mu(s)}{V_r(s)g(\hat{v}_\mu(s))} \iint_{\mathring{\mathscr{P}}} z(x,s)^T C_0 z(x,s)\, dx, \tag{A5}$$

since either $z(x,s) = 0$ on $\mathscr{L}$ or $\bar{v}_t(x,s) \cdot \hat{v}_{\partial\mathscr{P}}(x) = 0$ on $\mathscr{N}$. In this context, it should be also observed that the boundary term on the right-hand side of Equation (A5) is always positive, being by definition $\bar{v}_t(x,s) \cdot \hat{v}_{\partial\mathscr{P}}(x) > 0$ on $\mathscr{T}$. Using the fact that C_0 is positive definite, which gives $z(x,s)^T C_0 z(x,s) \geq \lambda_{\min}(C_0) z^2(x,s)$, the following inequality may hence be deduced:

$$\frac{1}{2}\frac{d}{ds}\|z(\cdot,s)\|^2_{L^2(\mathring{\mathscr{P}})} \leq \iint_{\mathring{\mathscr{P}}} z_x(x,s)\big(\sigma_x(s) - \varphi(s)y\big) + z_y(x,s)\big(\sigma_y(s) + \varphi(s)x\big)\, dx$$

$$- \frac{\hat{v}_\mu(s)}{V_r(s)g(\hat{v}_\mu(s))}\lambda_{\min}(C_0)\|z(\cdot,s)\|^2_{L^2(\mathring{\mathscr{P}})}. \tag{A6}$$

Using Hölder's and then Young's inequality for products yields

$$\iint_{\mathring{\mathscr{P}}} z_x(x,s)\big(\sigma_x(s) - \varphi(s)y\big)\, dx \leq \|z_x(\cdot,s)\|_{L^2(\mathring{\mathscr{P}})}\|\sigma_x(s) - \varphi(s)y\|_{L^2(\mathring{\mathscr{P}})}$$

$$\leq \frac{1}{2}\|z_x(\cdot,s)\|^2_{L^2(\mathring{\mathscr{P}})} + \frac{1}{2}\|\sigma_x(s) - \varphi(s)y\|^2_{L^2(\mathring{\mathscr{P}})}, \tag{A7a}$$

$$\iint_{\mathring{\mathscr{P}}} z_y(x,s)\big(\sigma_y(s) + \varphi(s)x\big)\, dx \leq \|z_y(\cdot,s)\|_{L^2(\mathring{\mathscr{P}})}\|\sigma_y(s) + \varphi(s)x\|_{L^2(\mathring{\mathscr{P}})}$$

$$\leq \frac{1}{2}\|z_y(\cdot,s)\|^2_{L^2(\mathring{\mathscr{P}})} + \frac{1}{2}\|\sigma_y(s) + \varphi(s)x\|^2_{L^2(\mathring{\mathscr{P}})}. \tag{A7b}$$

Combining Equation (A7a) with (A8) leads to

$$\frac{d}{ds}\|z(\cdot,s)\|^2_{L^2(\mathring{\mathscr{P}})} \leq \left(1 - \frac{2\hat{v}_\mu(s)}{V_r(s)g(\hat{v}_\mu(s))}\lambda_{\min}(C_0)\right)\|z(\cdot,s)\|^2_{L^2(\mathring{\mathscr{P}})}$$

$$+ \|\sigma_x(s) - \varphi(s)y\|^2_{L^2(\mathring{\mathscr{P}})} + \|\sigma_y(s) + \varphi(s)x\|^2_{L^2(\mathring{\mathscr{P}})}. \tag{A8}$$

Imposing $z(x,0) = z_0(x)$ (and thus also $z(x,0) = z_0(x)$), and recalling Grönwall–Bellman inequality finally yields the result (A2). ∎

Remark A.1: Proposition A.1 has been proved under the assumption of fixed contact patch. The proof may, however, be conducted similarly even for the case of time-varying contact patch, yielding exactly the same result as in Equation (A2) (see also [81]).

Remark A.2: If the approximated sliding velocity $\hat{v}_\mu(x,s)$ is assumed to also vary with x, but independently of $z(x,s)$, by observing that $\hat{v}_\mu(x,s)$ and the function $g(\cdot)$ are always nonnegative, it holds that

$$\iint_{\mathring{\mathscr{P}}} \frac{\hat{v}_\mu(x,s)}{V_r(s)g(v_\mu(x,s))} z(x,s)^T C_0 z(x,s)\, dx \geq 0, \tag{A9}$$

and therefore a simpler energy estimate for the total internal frictional state $z(x,s)$ may be derived exactly as for the classic brush tyre models, for example as done in [81].

Appendix 2. Analytical solutions

This appendix yields some analytical solutions for the results presented in Section 3.

A.1　Expressions for the α and β coefficients

The coefficients $\alpha_{xx}, \alpha_{xy}, \alpha_{yx}, \alpha_{yy}, \beta_x$ and β_y appearing in Equation (25) must satisfy

$$
\begin{bmatrix}
\varphi_{xx} & -\varphi_\gamma & 0 & \varphi_\psi + \varphi_{xy} & 0 & 0 \\
\varphi_\gamma & \varphi_{xx} & 0 & 0 & \varphi_\psi + \varphi_{xy} & 0 \\
-\varphi_\psi + \varphi_{yx} & 0 & 0 & \varphi_{yy} & \varphi_\gamma & 0 \\
0 & -\varphi_\psi & 0 & \varphi_\gamma & \varphi_{yy} & 0 \\
-1 & 0 & \varphi_{xx} & 0 & 0 & \varphi_\psi + \varphi_{xy} \\
0 & 0 & -\varphi_\psi + \varphi_{yx} & -1 & 0 & \varphi_{yy}
\end{bmatrix}
\begin{bmatrix}
\alpha_{xx} \\ \alpha_{xy} \\ \alpha_{yx} \\ \alpha_{yy} \\ \beta_x \\ \beta_y
\end{bmatrix}
=
\begin{bmatrix}
0 \\ -\varphi \\ \varphi \\ 0 \\ \sigma_x \\ \sigma_y
\end{bmatrix}.
\tag{A10}
$$

Solving the linear system in Equation (A10) yields the following expressions for the terms $\alpha_{xx}, \alpha_{xy}, \alpha_{yx}$ and α_{yy}:

$$
\alpha_{xx} = -\frac{\left(\varphi_\psi + \varphi_\gamma\right)\left(\varphi_{yy}^2 \varphi_\gamma + \varphi_{xx}\varphi_{yy}\varphi_\psi + \varphi_\psi^3 - \varphi_\psi^2 \varphi_\gamma - \varphi_\psi \varphi_\gamma^2 + \varphi_\gamma^3\right)}{\varphi_{xx}^2 \varphi_{yy}^2 + \varphi_{xx}^2 \varphi_\gamma^2 + 2\varphi_{xx}\varphi_{yy}\varphi_\psi^2 + \varphi_{yy}^2 \varphi_\gamma^2 + \varphi_\psi^4 - 2\varphi_\psi^2 \varphi_\gamma^2 + \varphi_\gamma^4},
\tag{A11a}
$$

$$
\alpha_{xy} = -\frac{\left(\varphi_\psi + \varphi_\gamma\right)\left(\varphi_{xx}\varphi_{yy}^2 + \varphi_{yy}\varphi_\psi^2 - \varphi_{yy}\varphi_\psi \varphi_\gamma - \varphi_{xx}\varphi_\psi \varphi_\gamma + \varphi_{xx}\varphi_\gamma^2\right)}{\varphi_{xx}^2 \varphi_{yy}^2 + \varphi_{xx}^2 \varphi_\gamma^2 + 2\varphi_{xx}\varphi_{yy}\varphi_\psi^2 + \varphi_{yy}^2 \varphi_\gamma^2 + \varphi_\psi^4 - 2\varphi_\psi^2 \varphi_\gamma^2 + \varphi_\gamma^4},
\tag{A11b}
$$

$$
\alpha_{yx} = \frac{\left(\varphi_\psi + \varphi_\gamma\right)\left(\varphi_{yy}\varphi_{xx}^2 + \varphi_{xx}\varphi_\psi^2 - \varphi_{xx}\varphi_\psi \varphi_\gamma - \varphi_{yy}\varphi_\psi \varphi_\gamma + \varphi_{yy}\varphi_\gamma^2\right)}{\varphi_{xx}^2 \varphi_{yy}^2 + \varphi_{xx}^2 \varphi_\gamma^2 + 2\varphi_{xx}\varphi_{yy}\varphi_\psi^2 + \varphi_{yy}^2 \varphi_\gamma^2 + \varphi_\psi^4 - 2\varphi_\psi^2 \varphi_\gamma^2 + \varphi_\gamma^4},
\tag{A11c}
$$

$$
\alpha_{yy} = -\frac{\left(\varphi_\psi + \varphi_\gamma\right)\left(\varphi_{xx}^2 \varphi_\gamma + \varphi_{yy}\varphi_{xx}\varphi_\psi + \varphi_\psi^3 - \varphi_\psi^2 \varphi_\gamma - \varphi_\psi \varphi_\gamma^2 + \varphi_\gamma^3\right)}{\varphi_{xx}^2 \varphi_{yy}^2 + \varphi_{xx}^2 \varphi_\gamma^2 + 2\varphi_{xx}\varphi_{yy}\varphi_\psi^2 + \varphi_{yy}^2 \varphi_\gamma^2 + \varphi_\psi^4 - 2\varphi_\psi^2 \varphi_\gamma^2 + \varphi_\gamma^4},
\tag{A11d}
$$

whilst the coefficients β_x, β_y may be factorised as $\beta_x = \tilde{\beta}_x/\tilde{\beta}, \beta_y = \tilde{\beta}_y/\tilde{\beta}$, with

$$
\begin{aligned}
\tilde{\beta}_x ={}& -\varphi_{yy}^3 \varphi_\gamma^2 - \sigma_y \varphi_\psi^5 - \varphi_{xx}\varphi_\psi^4 - \varphi_{yy}\varphi_\psi^4 - \varphi_{yy}\varphi_\gamma^4 + \sigma_x \varphi_{yy}\varphi_\psi^4 + \sigma_x \varphi_{yy}\varphi_\gamma^4 - \sigma_y \varphi_\psi \varphi_\gamma^4 \\
& -\varphi_{yy}\varphi_\psi \varphi_\gamma^3 + \varphi_{yy}\varphi_\psi^3 \varphi_\gamma - \varphi_{yy}^3 \varphi_\psi \varphi_\gamma + \sigma_x \varphi_{xx}^2 \varphi_{yy}^3 + \sigma_x \varphi_{yy}^3 \varphi_\gamma^2 + 2\sigma_y \varphi_\psi^3 \varphi_\gamma^2 - \varphi_{xx}\varphi_{yy}^2 \varphi_\psi^2 \\
& -\varphi_{xx}^2 \varphi_{yy}\varphi_\psi^2 + \varphi_{xx}\varphi_\psi^4 \varphi_\gamma^2 + 2\varphi_{yy}\varphi_\psi^2 \varphi_\gamma^2 - 2\sigma_y \varphi_{xx}\varphi_{yy}\varphi_\psi^3 - \varphi_{xx}\varphi_{yy}^2 \varphi_\psi \varphi_\gamma - \varphi_{xx}^2 \varphi_{yy}\varphi_\psi \varphi_\gamma \\
& + 2\sigma_x \varphi_{xx}\varphi_{yy}^2 \varphi_\gamma^2 - \sigma_y \varphi_{xx}^2 \varphi_{yy}^2 \varphi_\psi + \sigma_x \varphi_{xx}^2 \varphi_{yy}\varphi_\gamma^2 - \sigma_y \varphi_{xx}^2 \varphi_\psi \varphi_\gamma^2 - 2\sigma_x \varphi_{yy}\varphi_\psi^2 \varphi_\gamma^2 - \sigma_y \varphi_{yy}^2 \varphi_\psi \varphi_\gamma^2,
\end{aligned}
\tag{A12a}
$$

$$
\begin{aligned}
\tilde{\beta}_y ={}& \varphi_{xx}^2 \varphi_\psi^3 + 2\varphi_\psi^3 \varphi_\gamma^2 + \sigma_x \varphi_\psi^5 - \varphi_\psi \varphi_\gamma^4 - \varphi_\psi^5 + \sigma_y \varphi_{xx}\varphi_\psi^4 + \sigma_y \varphi_{xx}\varphi_\gamma^4 + \sigma_x \varphi_\psi \varphi_\gamma^4 - \varphi_{xx}\varphi_{yy}\varphi_\psi^3 \\
& + \varphi_{xx}^3 \varphi_{yy}\varphi_\psi + \varphi_{xx}\varphi_{yy}\varphi_\gamma^3 + \varphi_{xx}^3 \varphi_{yy}\varphi_\gamma + \sigma_y \varphi_{xx}^3 \varphi_{yy}^2 + \sigma_y \varphi_{xx}^3 \varphi_\gamma^2 - 2\sigma_x \varphi_\psi^3 \varphi_\gamma^2 - \varphi_{xx}^2 \varphi_\psi \varphi_\gamma^2 \\
& -\varphi_{yy}^2 \varphi_\psi \varphi_\gamma^2 - \varphi_{yy}^2 \varphi_\psi^2 \varphi_\gamma + 2\sigma_x \varphi_{xx}\varphi_{yy}\varphi_\psi^3 - 2\varphi_{xx}\varphi_{yy}\varphi_\psi^2 \varphi_\gamma + \sigma_x \varphi_{xx}^2 \varphi_{yy}^2 \varphi_\psi + 2\sigma_y \varphi_{xx}^2 \varphi_{yy}\varphi_\psi^2 \\
& + \sigma_y \varphi_{xx}\varphi_{yy}^2 \varphi_\gamma^2 + \sigma_x \varphi_{xx}^2 \varphi_\psi \varphi_\gamma^2 - 2\sigma_y \varphi_{xx}\varphi_\psi^2 \varphi_\gamma^2 + \sigma_x \varphi_{yy}^2 \varphi_\psi \varphi_\gamma^2,
\end{aligned}
\tag{A12b}
$$

and

$$
\tilde{\beta} = \left(\varphi_\psi^2 + \varphi_{xx}\varphi_{yy}\right)\left(\varphi_{xx}^2 \varphi_{yy}^2 + \varphi_{xx}^2 \varphi_\gamma^2 + 2\varphi_{xx}\varphi_{yy}\varphi_\psi^2 + \varphi_{yy}^2 \varphi_\gamma^2 + \varphi_\psi^4 - 2\varphi_\psi^2 \varphi_\gamma^2 + \varphi_\gamma^4\right).
\tag{A13}
$$

A.2　Analytical expression for steady-state initial conditions

The analytical expression for the steady-state solution $z^-(x)$ depends on the shape of the leading edge. The present appendix reports the closed-form expressions for the initial coordinates $x_0(\rho(x))$ in Equations (28a) and (30a) for a rectangular and an elliptical contact patch.

A.2.1 Rectangular contact patch

The contact patch is defined mathematically as

$$\mathscr{P} \triangleq \left\{ \boldsymbol{x} \in \Pi \mid -a \le x \le a, \; -b \le y \le b \right\}. \tag{A14}$$

The formal expressions for the initial conditions $\boldsymbol{x}_0(\boldsymbol{\rho}(\boldsymbol{x}))$ must be determined from three different parametrisations of the leading edge:

$$x = x_{\mathscr{L}_1}(y) = a, \quad y \in (-b, b), \tag{A15a}$$

$$y = y_{\mathscr{L}_2}(x) = b\,\mathrm{sgn}\varphi_\gamma, \quad x \in (0, a), \tag{A15b}$$

$$y = y_{\mathscr{L}_3}(x) = -b\,\mathrm{sgn}\varphi_\gamma, \quad x \in (-a, 0). \tag{A15c}$$

Introducing the function

$$\Gamma(\boldsymbol{x}) \triangleq x^2 + \left(y - 1/\varphi_\gamma\right)^2, \tag{A16}$$

and combining Equations (28a) with (A15a) yields

$$x_0\big(\boldsymbol{\rho}(\boldsymbol{x})\big) = a, \quad y_0\big(\boldsymbol{\rho}(\boldsymbol{x})\big) = \frac{1}{\varphi_\gamma} - \sqrt{\Gamma(\boldsymbol{x}) - R_0^2}\,\mathrm{sgn}\varphi_\gamma, \tag{A17a}$$

$$x_0\big(\boldsymbol{\rho}(\boldsymbol{x})\big) = \sqrt{\Gamma(\boldsymbol{x}) - R_1^2}, \quad y_0\big(\boldsymbol{\rho}(\boldsymbol{x})\big) = b\,\mathrm{sgn}\varphi_\gamma, \tag{A17b}$$

$$x_0\big(\boldsymbol{\rho}(\boldsymbol{x})\big) = -\sqrt{\Gamma(\boldsymbol{x}) - R_3^2}, \quad y_0\big(\boldsymbol{\rho}(\boldsymbol{x})\big) = -b\,\mathrm{sgn}\varphi_\gamma, \tag{A17c}$$

where

$$R_0 \triangleq a, \quad R_1 \triangleq b\,\mathrm{sgn}\varphi_\gamma - 1/\varphi_\gamma, \quad R_2 \triangleq \sqrt{R_1^2 + R_0^2},$$

$$R_3 \triangleq b\,\mathrm{sgn}\varphi_\gamma + 1/\varphi_\gamma, \quad R_4 \triangleq \sqrt{R_3^2 + R_0^2}. \tag{A18}$$

Substituting Equations (A17a) in (30a) provides three different expressions for the steady-state frictional state

$$\boldsymbol{z}_1^-(\boldsymbol{x}) = \tilde{\Phi}_{\varphi_\psi}\big(\Sigma_1(\boldsymbol{x}), 0\big)\boldsymbol{\Psi}_1(\boldsymbol{x}) + \tilde{\boldsymbol{z}}(\boldsymbol{x}), \quad (\boldsymbol{x}, s) \in \mathscr{P}_1^- \times \mathbb{R}_{\ge 0}, \tag{A19a}$$

$$\boldsymbol{z}_2^-(\boldsymbol{x}) = \tilde{\Phi}_{\varphi_\psi}\big(\Sigma_2(\boldsymbol{x}), 0\big)\boldsymbol{\Psi}_2(\boldsymbol{x}) + \tilde{\boldsymbol{z}}(\boldsymbol{x}), \quad (\boldsymbol{x}, s) \in \mathscr{P}_2^- \times \mathbb{R}_{\ge 0}, \tag{A19b}$$

$$\boldsymbol{z}_3^-(\boldsymbol{x}) = \tilde{\Phi}_{\varphi_\psi}\big(\Sigma_3(\boldsymbol{x}), 0\big)\boldsymbol{\Psi}_3(\boldsymbol{x}) + \tilde{\boldsymbol{z}}(\boldsymbol{x}), \quad (\boldsymbol{x}, s) \in \mathscr{P}_3^- \times \mathbb{R}_{\ge 0}, \tag{A19c}$$

where the functions $\Sigma_i(\cdot)$ and $\boldsymbol{\Psi}_i(\cdot)$ may be obtained using Equations (A17a), (A17b) or (A17c) in turn. The subdomains $\mathscr{P}_1^-$, $\mathscr{P}_2^-$, $\mathscr{P}_3^-$ represent the steady-state regions of three different portions of the contact patch:

$$\mathscr{P}_1 \triangleq \left\{ \mathscr{P} \setminus (\mathscr{P}_2 \cup \mathscr{P}_3) \right\}, \tag{A20a}$$

$$\mathscr{P}_2 \triangleq \left\{ \boldsymbol{x} \in \mathscr{P} \mid R_1^2 < \Gamma(\boldsymbol{x}) < R_2^2 \right\}, \tag{A20b}$$

$$\mathscr{P}_3 \triangleq \left\{ \boldsymbol{x} \in \mathscr{P} \mid R_3^2 < \Gamma(\boldsymbol{x}) < R_4^2, \; x < 0 \right\}, \tag{A20c}$$

and therefore

$$\mathscr{P}_1^- \triangleq \left\{ \boldsymbol{x} \in \mathscr{P}_1 \mid \gamma_{\Sigma_1}(\boldsymbol{x}, s) < 0 \right\}, \quad \mathscr{P}_1^+ \triangleq \left\{ \boldsymbol{x} \in \mathscr{P}_1 \mid \gamma_{\Sigma_1}(\boldsymbol{x}, s) \ge 0 \right\}, \tag{A21a}$$

$$\mathscr{P}_2^- \triangleq \left\{ \boldsymbol{x} \in \mathscr{P}_2 \mid \gamma_{\Sigma_2}(\boldsymbol{x}, s) < 0 \right\}, \quad \mathscr{P}_2^+ \triangleq \left\{ \boldsymbol{x} \in \mathscr{P}_2 \mid \gamma_{\Sigma_2}(\boldsymbol{x}, s) \ge 0 \right\}, \tag{A21b}$$

$$\mathscr{P}_3^- \triangleq \left\{ \boldsymbol{x} \in \mathscr{P}_3 \mid \gamma_{\Sigma_3}(\boldsymbol{x}, s) < 0 \right\}, \quad \mathscr{P}_3^+ \triangleq \left\{ \boldsymbol{x} \in \mathscr{P}_3 \mid \gamma_{\Sigma_3}(\boldsymbol{x}, s) \ge 0 \right\}. \tag{A21c}$$

Both in transient and steady-state conditions, the complete solution over the whole contact patch is not $C^1(\mathring{\mathscr{P}} \times \mathbb{R}_{>0}; \mathbb{R}^2)$ nor $C^0(\mathscr{P} \times \mathbb{R}_{\ge 0}; \mathbb{R}^2)$. Indeed, the continuity between the regions $\mathscr{P}_1$ and

$\mathscr{P}_2$ stems directly from the fact that the value assumed by the bristle deflection at $x = x_{\mathscr{L}_1}(y) = a$ is the same for both Equations (A19a) and (A19b). In contrast, the continuity of the solution is not preserved on $\mathcal{C}_3(\boldsymbol{x})$.

A.2.2 Elliptical contact patch

An elliptical contact patch is described as the set

$$\mathscr{P} \triangleq \left\{ \boldsymbol{x} \in \Pi \,\middle|\, \frac{x^2}{a^2} + \frac{y^2}{b^2} \leq 1 \right\}, \tag{A22}$$

with the leading edge parametrised by

$$x = x_{\mathscr{L}}(y) = a\sqrt{1 - \frac{y^2}{b^2}}, \quad y \in (-b, b). \tag{A23}$$

Setting $y_0(\boldsymbol{\rho}) = \rho_2$ and $x_0(\boldsymbol{\rho}) = x_{\mathscr{L}}(\rho_2)$ yields the following expression for the composite function $y_0(\boldsymbol{\rho}(\boldsymbol{x}))$:

$$y_0\big(\boldsymbol{\rho}(\boldsymbol{x})\big) = \frac{\frac{1}{\varphi_\gamma} - \sqrt{\frac{1}{\varphi_\gamma^2} - \left(1 - \frac{a^2}{b^2}\right)\left(\frac{1}{\varphi_\gamma^2} + a^2 - \Gamma(\boldsymbol{x})\right)}\,\mathrm{sgn}\varphi_\gamma}{\left(1 - \frac{a^2}{b^2}\right)}, \tag{A24}$$

where $\Gamma(\cdot)$ is defined as in Equation (A16). Accordingly, the initial condition for the longitudinal coordinate clearly becomes $x_0(\boldsymbol{\rho}(\boldsymbol{x})) = x_{\mathscr{L}} \circ y_0(\boldsymbol{\rho}(\boldsymbol{x}))$, with $x_{\mathscr{L}}(\cdot)$ reading as in Equation (A23). It is worth mentioning that Equation (A24) is valid under the assumption that $a^2 \leq b(b + 1/|\varphi_\gamma|)$ [59].

Appendix 3. Classic formulation of the LuGre-brush tyre models

The classic formulation of the LuGre-brush tyre models approximates the tangential velocity field with the rolling velocity of the tyre, that is $\bar{\boldsymbol{v}}_t \approx -\hat{\boldsymbol{e}}_x$, neglects the contribution of the internal friction state to the turning speed ($\chi_\psi = 0$), and considers a diagonal matrix $\mathbf{C}_0$, that is $c_{0xy} = c_{0yx} = 0$ by assumption.

Owing to these premises, and replacing the time variable t with the travelled distance s, the steady-state and transient solutions for the internal frictional state $\boldsymbol{z}(\boldsymbol{x}, s)$ may be sought using the method of characteristic lines, as done already in Section 3. However, in this case, it is customary to consider a proper change of coordinates:

$$\boldsymbol{\xi} = \begin{bmatrix} \xi \\ \eta \end{bmatrix} \triangleq \begin{bmatrix} x_{\mathscr{L}}(y) - x \\ y \end{bmatrix}, \tag{A25}$$

where $x = x_{\mathscr{L}}(y)$ is a parametrisation of the leading edge in the original space variables $\boldsymbol{x}$. It is worth emphasising that the above transformation given by Equation (A25) may be used only when the contact patch is fixed. With the change of coordinates in Equation (A25), the steady-state solution may be more conveniently expressed in components as

$$z_x^-(\boldsymbol{\xi}) = \lambda_x(\sigma_x - \varphi\eta)\left(1 - \mathrm{e}^{-\frac{\xi}{\lambda_x}}\right), \quad (\boldsymbol{\xi}, s) \in \mathscr{P}^- \times \mathbb{R}_{\geq 0}, \tag{A26a}$$

$$z_y^-(\boldsymbol{\xi}) = \lambda_y\Big[\sigma_y + \varphi\big(x_{\mathscr{L}}(\eta) + \lambda_y\big)\Big]\left(1 - \mathrm{e}^{-\frac{\xi}{\lambda_y}}\right) - \lambda_y\varphi\xi, \quad (\boldsymbol{\xi}, s) \in \mathscr{P}^- \times \mathbb{R}_{\geq 0}, \tag{A26b}$$

where

$$\lambda_x \triangleq \frac{V_\mathrm{r}g(\hat{v}_\mu)}{\hat{v}_\mu c_{0xx}} \equiv \frac{1}{\varphi_{xx}} \quad \text{and} \quad \lambda_y \triangleq \frac{V_\mathrm{r}g(\hat{v}_\mu)}{\hat{v}_\mu c_{0yy}} \equiv \frac{1}{\varphi_{yy}} \tag{A27}$$

may be easily interpreted as the longitudinal and lateral relaxation lengths. Similarly, the components for the transient solution $z^+(\boldsymbol{\xi}, s)$ read

$$z_x^+(\boldsymbol{\xi}, s) = \lambda_x(\sigma_x - \varphi\eta)\left(1 - \mathrm{e}^{-\frac{s}{\lambda_x}}\right) + z_{x0}(\xi - s, \eta)\mathrm{e}^{-\frac{s}{\lambda_x}}, \quad (\boldsymbol{\xi}, s) \in \mathscr{P}^+ \times \mathbb{R}_{\geq 0}, \qquad \text{(A28a)}$$

$$z_y^+(\boldsymbol{\xi}, s) = \lambda_y\Big[\sigma_y + \varphi\big(x_{\mathscr{L}}(\eta) - \xi + \lambda_y\big)\Big]\left(1 - \mathrm{e}^{-\frac{s}{\lambda_y}}\right) + \big(z_{y0}(\xi - s, \eta) - \lambda_y\varphi s\big)\mathrm{e}^{-\frac{s}{\lambda_y}},$$

$$(\boldsymbol{\xi}, s) \in \mathscr{P}^+ \times \mathbb{R}_{\geq 0}. \qquad \text{(A28b)}$$

It should be noticed that the analytical expressions in Equations (A28a) do not appear in previous works. A rapid inspection also confirms that $z^+(\boldsymbol{\xi}, \xi) \equiv z^-(\boldsymbol{\xi})$, since the curve $\gamma_\Sigma \triangleq \xi - s = 0$ parametrises a travelling edge. Therefore, using the coordinates $\boldsymbol{\xi}$, the steady-state and transient regions of the contact patch are described by $\mathscr{P}^- = \{\boldsymbol{\xi} \in \mathscr{P} \mid \xi - s < 0\}$ and $\mathscr{P}^+ = \{\boldsymbol{\xi} \in \mathscr{P} \mid \xi - s \geq 0\}$, respectively. In this case, the classic rectangular and elliptical contact patches are both convex in the rolling direction $\bar{\boldsymbol{\nu}}_t = -\hat{\boldsymbol{e}}_x$, implying that $z(\boldsymbol{\xi}, s) \in C^0(\mathscr{P} \times \mathbb{R}_{\geq 0}; \mathbb{R}^2)$.